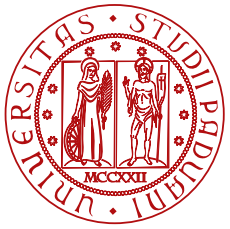

Università degli Studi di Padova

Dipartimento di Ingegneria dell'Informazione

Master Thesis in ICT for Internet and Multimedia - Telecommunications

Probe Array Antenna System: an extension of the current technology to cope with different DUT sizes, single-channel instrumentation and a novel method to evaluate the DUT receiving properties

Master Candidate

Mattia Piana

Student ID 2053041

Supervisor

Prof. Marco Santagiustina

University of Padova

Co-supervisor

Dott. Thomas Deckert

NI

Academic Year 2022-2023

Graduation Date 24 Oct 2023

To my family

Abstract

This work is focused on the Probe Array Antennas System: a novel over-the-air approach able to estimate the far field pattern of an antenna via near field measurements. My contribution can be summarized as an extension of the current technology both theoretical and practical, allowing the system to work with variable DUT sizes, single-channel instrumentation, and an increase of the measurement speed.

Contents

List of Figures

List of Tables

List of Acronyms

DUT Device Under Test

NI National Instruments

TUD Technische Universität Dresden

FF Far Field

NF Near Field

PAS Probe Array System

EIRP Effective Isotropic Radiated Power

RF Radio Frequency

VST Vector Signal Transceiver

SG Signal Generator

SA Signal Analyzer

1

Introduction

One of the 5G requirements is an enhanced datarate, that will demand the use of new portions of spectrum so far left unused [1]. In fact, according to [20] the 5G technologies will mainly operate in the 28 GHz frequency band or above, with channel bandwidth around or above 1 GHz. This will allow to have antenna on chip and antenna on package systems due to the reduced wavelength, and so very small but powerful devices. According to [28] the new 5G requirements demand a complex testing structure as depicted in Fig.1.1.

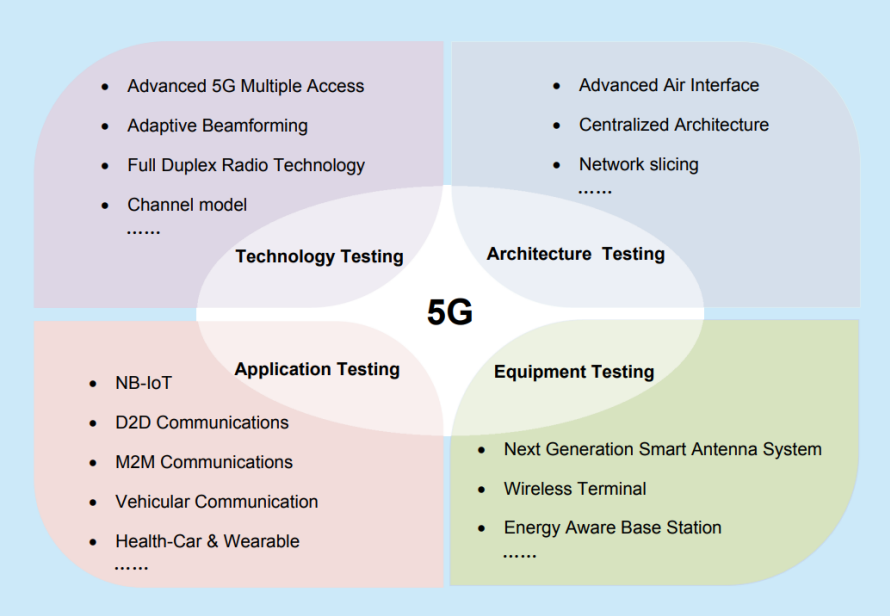

Figure 1.1: 5G testing schema

We can refer to that schema and divide the testing requirements in:

- New Air Interface
- Channel
- Network Architecture
- Antenna System

New Air Interface

The objective of air interface of 5G is to achieve higher transmission rate, flexible access ways, improved spectral efficiency and better user experience [13]. The way this is done is via waveform, channel coding, non-orthogonal multiple access, as well as massive multi-antenna techniques [4]. Compared to 4G, new waveforms have been proposed to enhance the spectral efficiency and band sharing between different services.

Channel

Massive MIMO and mmWave frequencies are the key enablers for 5G in terms of high datarate, spectral efficiency and capacity. These technologies demand further research on channel characteristics to exploit their potential. In particular, for what concernes the massive MIMO channel, as the number of antennas increases the user equipment and scatterers are more likely to be found within the Rayleigh distance and this means that the wave front cannot be assumed plane but spherical. This is because the Rayleigh distance is proportional to the square of the antenna dimension, and as the number of antennas increases also the array dimension does as well. A spherical plane wave increases the complexity of the channel modeling; in [24] a simulation of the impact on the capacity of different channel models assumptions is studied. It shows that plane wave and spherical wave assumptions behave differently especially in the near-field region, while they converge in the far field. In [15] a second order approximation of the spherical wave front (i.e., parabolic wave front) is studied and validated via numerical simulation. According to the Friis formula, the higher the frequency the higher the attenuations due to the pathloss. This is true when assuming the antenna gain to be constant over frequency. If the physical size of the antenna (e.g., effective aperture) is kept constant over frequency at both

link ends and the atmosphere is clear, then path loss in free space actually decreases quadratically as frequency increases [21]. Moreover, additional effects due to the absorption by the atmosphere and penetration loss need to be taken into account. In order to cope with these additional phenomena, measurements in both line-of-sight and non-line-of-sight scenarios for future outdoor cellular systems at 28 GHz and 38 GHz were conducted in urban micro-cellular environments in New York City and Austin, Texas, respectively [16]. The aim of the study was to provide cell designers with simple yet effective path loss models. Adaptive beam steerable antenna arrays are exploited to overcome these losses, at the expense of more complicated antenna systems.

Network Architecture

5G network architecture will not only use some technologies of 4G, but also adopt some new solutions and technologies. Compared to 4G, the new standard aims to dinamically tailor its capabilities to the user requirements and this requires also changes on the network architecture as we can observe in Fig. 1.2.

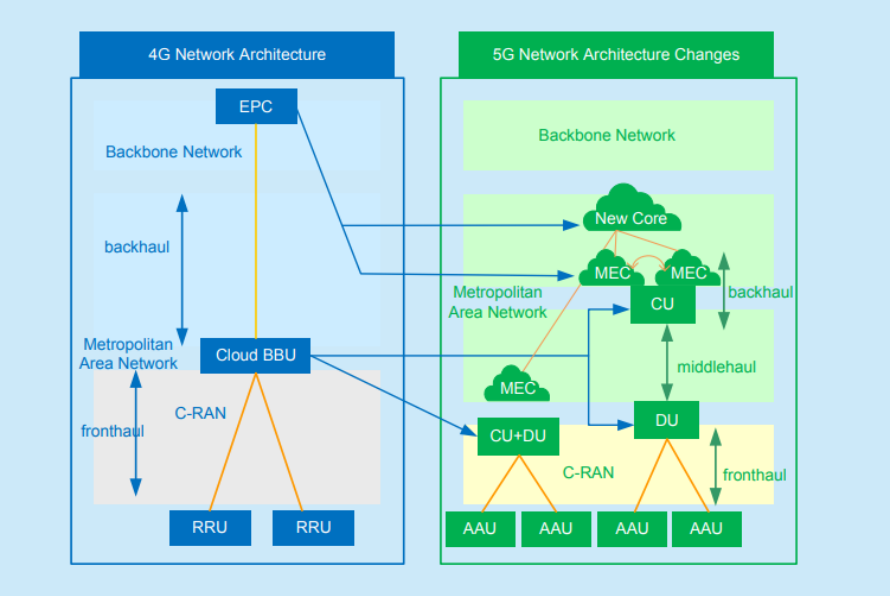

Figure 1.2: 4G VS 5G: network architecture

As we can see, one of the main differences between 4G and 5G networks is that in the latter there is the tendency to bring network functionalities closer to the end user. This is the key enabling to mobile-edge-computing: bringing the

core features to the edge network has an impact on the latency and the efficiency of the system. The 5G network architecture went through some vendors tests aimed to evaluate:

- Network slicing: virtualization platform test and performances evaluations
- MEC: proving that the proposed network function placements reduces latency
- CP/UP separation: verify that the Control Plane and User Plane interface solution works properly

Antenna System Testing

Antenna system testing is an essential step of the radio performance evaluation. Conducted testing has been widely used before 4G, and it consists of replacing the antennas with RF cables. In many cases, for the 5G communication systems, OTA (Over-The-Air) testing is the only way for practical RF system evaluations as:

1. Millimeter wave systems are so compact that there is no room for a standard connector as it is not possible to fit in an RF connector between the antenna and the radio systems. In fact the chipsets exploited usually do not have RF connector to support any conducted measurement.
2. Even if there were such connectors, the number and overall complexity of coaxial cable connections to test these devices would increase impractically high as a massive MIMO is one of the major enabler of 5G [27][28] [23].
3. The antenna array signal processing, e.g., beamforming, null steering, cannot be evaluated in the conducted setup [28]

Compared to the conducted testing, OTA has a great advantage, i.e. it can reproduce desired channel environment in a controllable, debuggable and repeatable way.

OTA testing is the main theme of this thesis. In fact, I had the opportunity to work on the topic as an intern at NI (National Instruments) in Dresden (Germany) for six months. The thesis is the product of such a wonderful and formative experience. After this brief introduction and justification, in the next section the State of the Art of OTA testing is presented.

1.1 State of the Art

Antennas systems need to be tested where they will be supposed to operate, i.e. in their Far Field condition. There are basically two ways in which OTA testing is performed: *chamber based* and *NF-FF techniques*. The main difference between the two is that in the former case, the measurements to test the device are performed in its FF and so we can "directly" use the measurements data to infer FF properties (e.g. radiation pattern, EIRP, ecc...). On the contrary, in the latter case, NF measurements are exploited to evaluate the DUT FF properties and so an additional processing needs to be performed on the NF data to recover FF informations.

1.1.1 Chamber Based OTA Testing

The chamber based OTA testing approach usually consists of an anechoic chamber that provides a controlled environment. Due to the small wavelength (few millimeters) at the frequency at which these new 5G devices will be operating, the 5G chambers are much smaller compared to the 4G chambers. We are talking about 1-2 meters versus tens of meters. Inside, these chambers are covered by absorbers in order to limit the signal reflections and so evaluate the radiation pattern of the DUT by means of probe(s) located in the FF. At NI there is a mmWave Chamber [1] specifically designed to operate up to 60 GHz (to be more precise, the chamber can go even beyond 60 GHz but the probes, cables and connectors don't support higher frequencies). In figure 1.3 the FF measurement setup is shown.

[1] https://en.zhbojay.com/shepin-ceshi-jiejue-fangan/bj-8019.html

(a) Bojay 8019 (outside view)

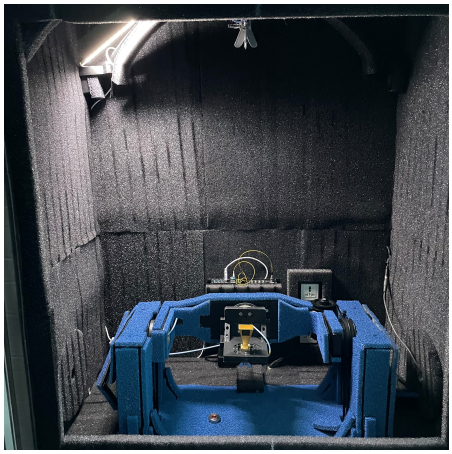

(b) Bojay 8019 (inside view)

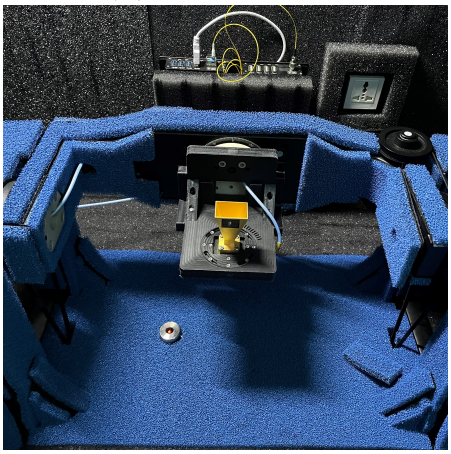

(c) Moving positioner and Horn Antenna under test

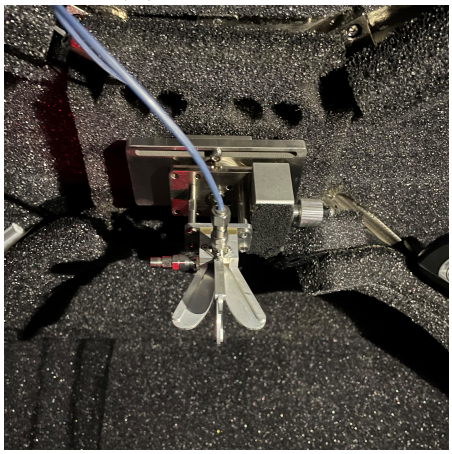

(d) Probe antenna: Quad-Ridged Horn Antenna RFSpin QRH50

Figure 1.3: FF measurement setup at NI

Another type of chamber based OTA test is the so called *reverberation chamber*. The reverberation chamber is a large metal cavity provided with mode stirrers and one or more antennas that will emulate Rayleigh fading when the modes are stirred [8]. This is because due to the multiple reflections the device will receive plane waves with a omni-directional distribution of angles of arrival [22]. The main advantage of the reverberation chamber versus the anechoic chamber is that it is smaller and cheaper, and that the measurements take shorter time. Still, anechoic and reverberation chambers have different use cases: the former aims to characterize the antenna under test, the latter the behavior of the device in real world environments in absence of LOS (Line of Sight) path. Still, according to [9] we will probably use anechoic chambers with steerable lobes to test terminals, radio links and base stations in mmWave 5G systems. This is because it is no

longer expected to have i.i.d channels on the antennas ports like in 4G due to the path-loss. In fact, as we can see in figure 1.4, at mmWave frequencies steerable lobes are needed. This results in a change on the channel statistic, which cannot be assumed as an i.i.d Gaussian random variable across the antennas. The 5G anechoic test concept is called Random-LOS because one side of the link may be subject to randomness causing a random Angle-of-Arrival (AoA) and quite often also randomness in polarization.

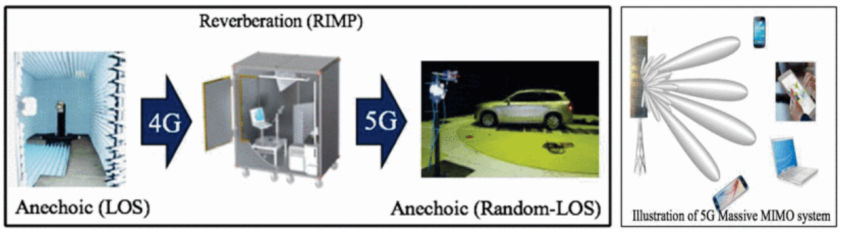

Figure 1.4: Chamber based OTA Test shifting

Another way in which one can characterize the DUT behavior in different scenarios is the *Multi-probe* anechoic chamber [10]. This technique uses an anechoic chamber and makes it suitable for testing the DUT at different channels via multiple probes. Given a target channel condition (i.e., angle of arrivals, delay spread ecc...), the probes are driven accordingly to reproduce that.

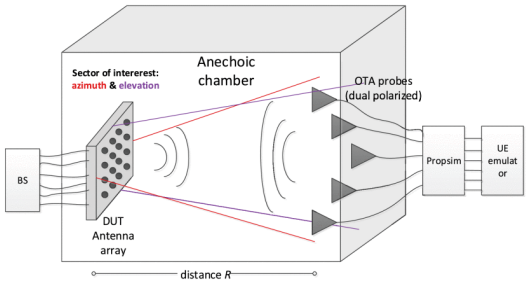

Figure 1.5: MPAC reference schema

A variation of the previous method is the *Ultra Compact PWG Chamber* [5]. The Ultra Compact PWG chamber system, depicted in Fig.1.6, is intended to make the test setup as small and compact as possible in production test scenarios. It

exploits multiple probes in order to create a virtual far field by means of a so called PWG (Planar Wavefront Generator). Performance parameters of the DUT, such as radiation pattern, EIRP and spurious emissions can be characterized in a similar way as had the DUT been located in a far field chamber, although the size of the PWG Ultra Compact Chamber is much smaller.

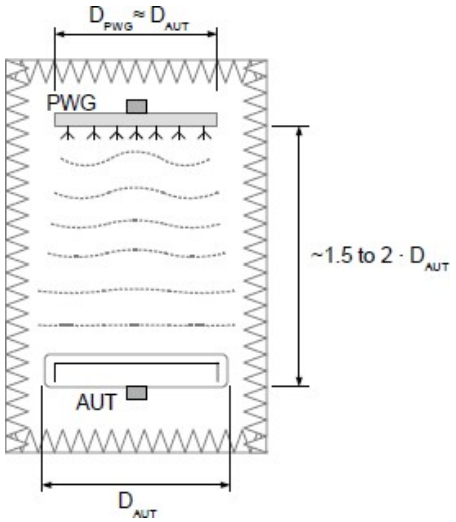

Figure 1.6: MPAC reference schema

There is also a fourth option which can be seen as a combination between fully anechoic and reverberation chambers. This kind of chamber is referred as CATR that stands for *Compact Antenna Test Range*. It exploits either reflectometers [25] or lenses [6] in order to reach the DUT FF condition (i.e., plane waves impacting on the device) within limited distances. There are several trade-offs between the direct FF tests (i.e., the anechoic chamber) and the CATR systems. The main advantages of the CATR is that allows to test the DUT in smaller spaces compared to the anechoic chambers and also the path loss is reduced, allowing a larger dynamic range. The first limitation is that it has usually smaller quiet zones (i.e., regions in space where we can place the DUT as we know that the wave propagation properties are sufficiently good) since it is limited by the reflectometer/lens aperture. The second limitation is that there are ripples in the wave front due to imperfections of the surfaces. This might be the major problem in testing mmWave devices, as the higher the frequency the smoother the surfaces need to be.

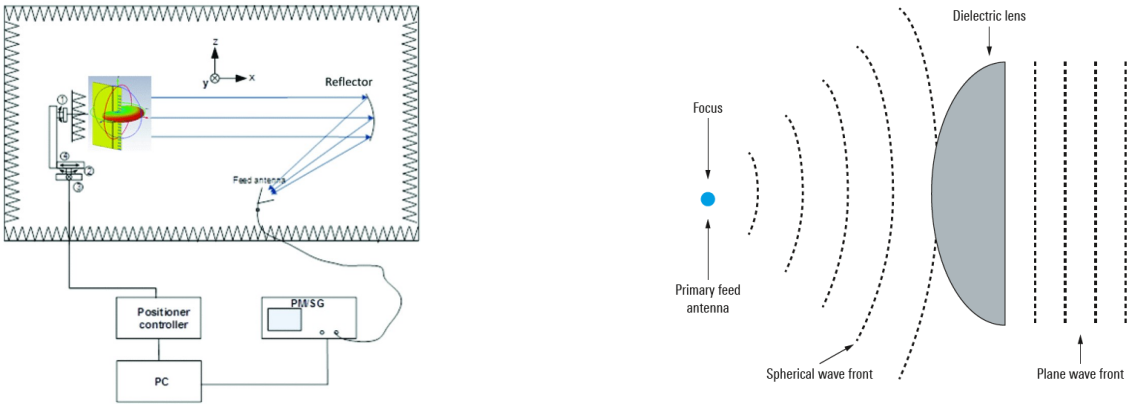

(a) CATR system with reflectometer (b) Use of a lens to generate plane waves

Figure 1.7: CATR system

1.1.2 NF OTA Testing Techniques

The evolution of the near-field scanning as a method for measuring antennas can be divided into four periods: the early experimental period with no probe correction (1950-1961), the period of the first probe-corrected theories (1961-1975), the period in which the first theories were put into practice (1965-1975), and the period of technology transfer (1975-1985) in which 50 or more near-field scanners were built throughout the world [26]. In figure 1.8 a classification based on the properties of the fields emitted by a generic antenna is depicted. The *Reactive near-field* region is defined as that portion of the near-field region immediately surrounding the antenna where the reactive field predominates. For most antennas, the outer boundary of this region is considered to be at a distance $R < 0.62\sqrt{D^3/\lambda}$ from the antenna surface. Here, D is the maximum dimension of the emitting antenna. The *Radiating near-field* (Fresnel) region is defined as that region of the field of an antenna between the reactive near-field region and the far-field region where radiation fields predominate and where the angular field distribution is dependent upon the distance from the antenna. The inner boundary is taken to be the distance $R \geq 0.62\sqrt{D^3/\lambda}$ and the outer boundary the distance $R < 2D^2/\lambda$. This criterion is based on a maximum phase error of $\pi/8$ from the plane wave assumption. In the radiating near-field region the field pattern is, in general, a function of the radial distance and the radial field component is not negligible. The *Far-field* (Fraunhofer) region is defined as that region of the field of an antenna where the angular field distribution is

essentially independent of the distance from the antenna. In other words, the distance from the emitting antenna does not change the shape of the radiation pattern but only scales it down due to the path loss. It is usually defined for distances $R \geq 2D^2/\lambda$ from the emitting antenna. That is the region where the antennas are meant to operate, and so the most interesting for most of the use cases.

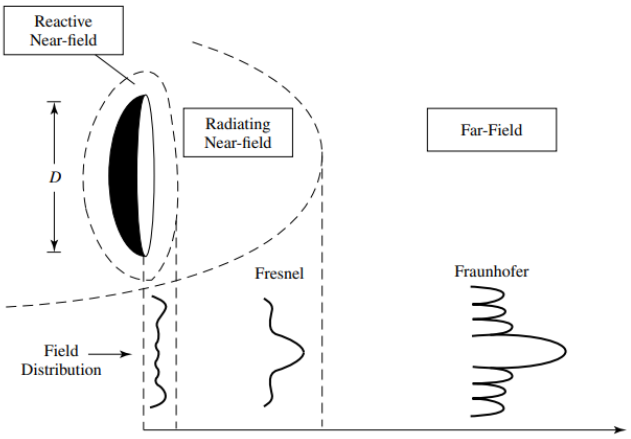

Figure 1.8: Fields Classification [2]

As explained in [2], there is a well known technique to reconstruct the FF electric field emitted by an antenna via NF measurements. In fact, there is a deterministic transformation based on a spatial 2D Fourier Transform that allows us to pass from NF to FF. We can write the electric field emitted by a generic antenna as a sum of plane waves propagating in different directions:

$$\boldsymbol{E}(x,y,z) = \frac{1}{4\pi^2}\int_{-\infty}^{+\infty}\int_{-\infty}^{+\infty} \boldsymbol{f}(k_x,k_y)e^{-j(\boldsymbol{k}\cdot\boldsymbol{r})}\,dk_x\,dk_y \tag{1.1}$$

Once the function $\boldsymbol{f}(k_x,k_y)$ (i.e., the *modal expansion*) is known, we are then able to weight each plane wave $e^{-j(\boldsymbol{k}\cdot\boldsymbol{r})}$ in eq. (1.1) and so reconstruct the electric field $\boldsymbol{E}(x,y,z)$ in an arbitrary position in the space (reactive region excluded). If we pick a generic position in the NF (for simplicity, let us fix the plane $z = 0$) equation (1.1) can be further simplified. Doing so the electric field components tangential to the surface $z = 0$ are

$$E_x(x,y,z=0) = \frac{1}{4\pi^2}\int_{-\infty}^{+\infty}\int_{-\infty}^{+\infty} f_x(k_x,k_y)e^{-j(k_x x+k_y y)}\,dk_x\,dk_y \tag{1.2}$$

$$E_y(x, y, z = 0) = \frac{1}{4\pi^2} \int_{-\infty}^{+\infty} \int_{-\infty}^{+\infty} f_y(k_x, k_y) e^{-j(k_x x + k_y y)}\, dk_x\, dk_y \tag{1.3}$$

We can notice that, by taking the inverse Fourier Tranform of equations (1.2) and (1.3) we are able to calculate components x and y of the modal spectrum as:

$$f_x(k_x, k_y) = \int_{-\infty}^{+\infty} \int_{-\infty}^{+\infty} E_x(x, y, z = 0) e^{j(k_x x + k_y y)}\, dx\, dy \tag{1.4}$$

$$f_y(k_x, k_y) = \int_{-\infty}^{+\infty} \int_{-\infty}^{+\infty} E_y(x, y, z = 0) e^{j(k_x x + k_y y)}\, dx\, dy \tag{1.5}$$

It can be shown [2] that we can reconstruct the FF in polar coordinates via the NF modal spectrum $f_x(k_x, k_y)$ and $f_y(k_x, k_y)$:

$$E_{\theta,FF}(r, \theta, \phi) \simeq j \frac{k e^{jkr}}{2\pi r} [f_x(\theta, \phi) cos(\phi) + f_y(\theta, \phi) sin(\phi)] \tag{1.6}$$

$$E_{\phi,FF}(r, \theta, \phi) \simeq j \frac{k e^{jkr}}{2\pi r} cos(\theta) [-f_x(\theta, \phi) sin(\phi) + f_y(\theta, \phi) cos(\phi)] \tag{1.7}$$

There are few remarks that are worth mentioning here for practical implementations. Firstly, in order to practically implement equations (1.2) and (1.3) we can limit the integrals on a surface where the tangential components of the fields are significantly different from zero, moreover we cannot perform a continuous sampling to measure those fields. In order to avoid aliasing, we need to sample at a distance less or equal to $\frac{\lambda}{2}$. Ultimately, in the sampling procedure the effect that the probe has on the measurement needs to be taken into account. In fact due to the inherent directivity of the probe the samples further away from the phase centre of the DUT will be attenuated compared to the samples close to the centre. This effect needs to be mitigated and is called probe compensation. There are different techniques to achieve that, one is the "Square Root Method" [18] in which the probe correction coefficients are found by measuring a probe on a NF range with an identical probe and taking the square root of the transformed FF. We can see the previous technique as a special case of a more general NF scanning theory explained in [26]. In fact the far electric field is given by a vector Kirckhoff integral eq. (1.8):

$$\boldsymbol{E}(\boldsymbol{r}) = \frac{-ike^{ikr}}{4\pi r}\hat{\boldsymbol{r}} \times \oint_S (\boldsymbol{K}_m + Z_0\hat{\boldsymbol{r}} \times \boldsymbol{K}_e)e^{-ik\hat{\boldsymbol{r}}\cdot\boldsymbol{r}'}\, dS' \tag{1.8}$$

where: $\boldsymbol{K}_e = \hat{\boldsymbol{n}} \times \boldsymbol{H}$, $\boldsymbol{K}_m = -\hat{\boldsymbol{n}} \times \boldsymbol{E}$ and $r \to \infty$. In words, what equation (1.8) is saying is that we can calculate the electric field at infinity (i.e., in the far field) by enclosing the antenna on an arbitrary surface S and measuring the electric and magnetic fields tangential to that surface (see Fig. 1.9).

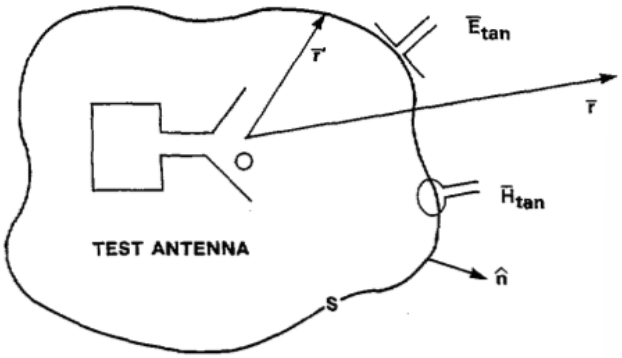

Figure 1.9: Integration surface S surrounding the antenna under Test, with tangential Electric and Magnetic fields

Since to apply (1.8) one should measure both magnetic and electric fields, it is possible to rewrite that in terms of only the electric (or magnetic) field, leading to:

$$\boldsymbol{E}(\boldsymbol{r}) = \oint_S [\hat{\boldsymbol{n}}' \times \boldsymbol{E}(\boldsymbol{r}')] \cdot G(\boldsymbol{r}, \boldsymbol{r}')\, dS' \tag{1.9}$$

where G is the dyadic Green's function, which is pretty much dependent on the geometry of the surface S. The estimation of G is impractical for a generic surface S, but for some with certain properties it is feasible. One can refer to [19] (chp. 13) to have a more detailed explanation. The surfaces that are used in practice, both for good mathematical properties as well as practical feasibility (we need a probe to scan in the NF those surfaces) are the planar, spherical and cylindrical ones. The specific eigenfunction expansions for planar, cylindrical, and spherical scanning, along with their inverse orthogonality integrations for the transmission coefficients are given in Fig. 1.10. We can notice that the planar expression is exactly the one previously found in equations (1.2)-(1.5) with $z_0 = 0$ and $\gamma = 0$.

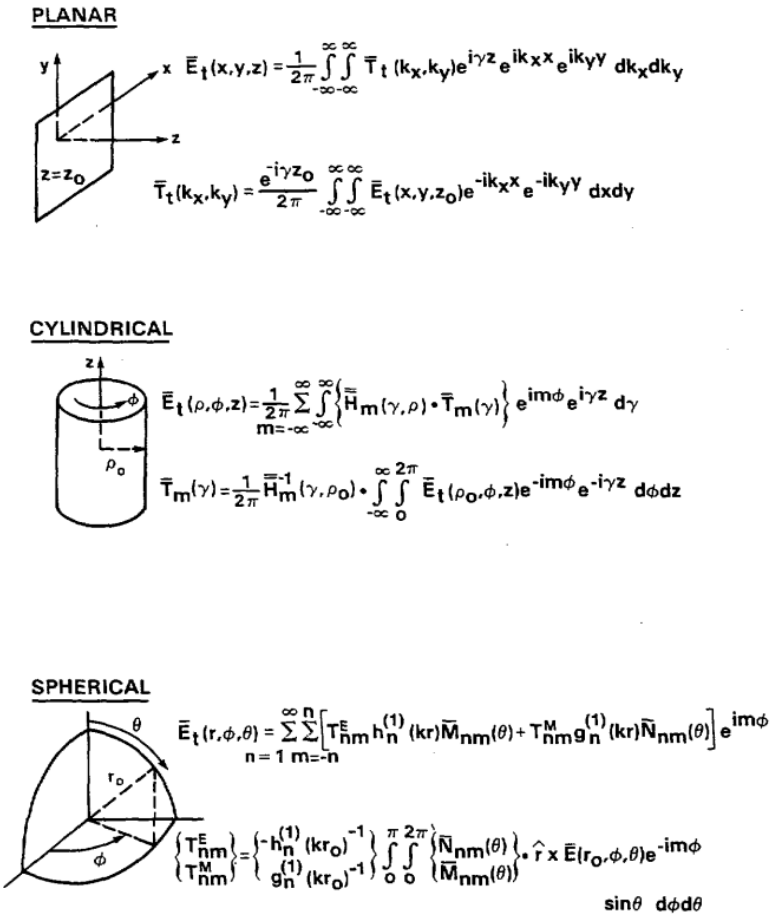

Figure 1.10: Fields Classification [2]

1.2 Thesis Organization

After this brief introduction on why OTA testing is important and which are the main options to carry it out, in this section an outline of the work I carried out during my internship is presented. The topic of the internship is the PAS, namely a novel NF technique different from those presented in the State of The Art section. In Chapter 2, a system description of the PAS technology is given as well as the hardware/DUTs used to perform the measurements. Then, the measurement model derivation for the TX testing is explained as well as the core algorithm used to process the NF data to obtain FF indications. In section 2.3 we present the derivation of the model used for RX testing and the algorithm used at the current implementation to process the NF data to reconstruct the DUT sensitivity pattern, as well as the performance of such

algorithm. In Chapter 3 a study on the scalability of the PAS to different DUT sizes is performed. In particular different DUTs are measured with PASs that are not specifically designed for them, because one of the objective is to design a system independent of the DUT structure. In Chapter 4 a novel algorithm for the RX testing is explained and assessed. That algorithm was developed and implemented by Martin Obermaier (PhD candidate at TU Dresden) and myself during the internship period, and speeds up the system in all the cases where the number of points of the sensitivity pattern we are interested in is less than the number of DUT's antennas. In Chapter 5 an extension of the current technology is presented, aiming to decrease the necessary hardware (and so the cost) of the system. The idea is to exploit a beam former at PAS side and perform measurements at multiple times instead of in parallel, a solution that would require multiple instruments driven simultaneously. In Chapter 6 there is a summary of the outcomes of the previous chapters as well as an indication of the next steps to further develop the technology. In the Appendix A a more rigorous mathematical justification on the PAS measurement model and TX reconstruction algorithm is given. Even though it is not mandatory for the understanding of the whole system, it gives some useful remarks and insights for the practical implementation. In the Appendix B a second algorithm for the DUT TX characterization called Simple Calibration Algorithm is given. The word "Simple" refers to the mathematical structure involved, but in terms of computational time and resources is perfectly equivalent to that presented in Chapter 2.

2

The Near-field Probe Array System

The Probe Array System (PAS) is a novel over the air approach to estimate the antenna characteristics (radiation pattern, EIRP,...) via near field measurements [14] [11].

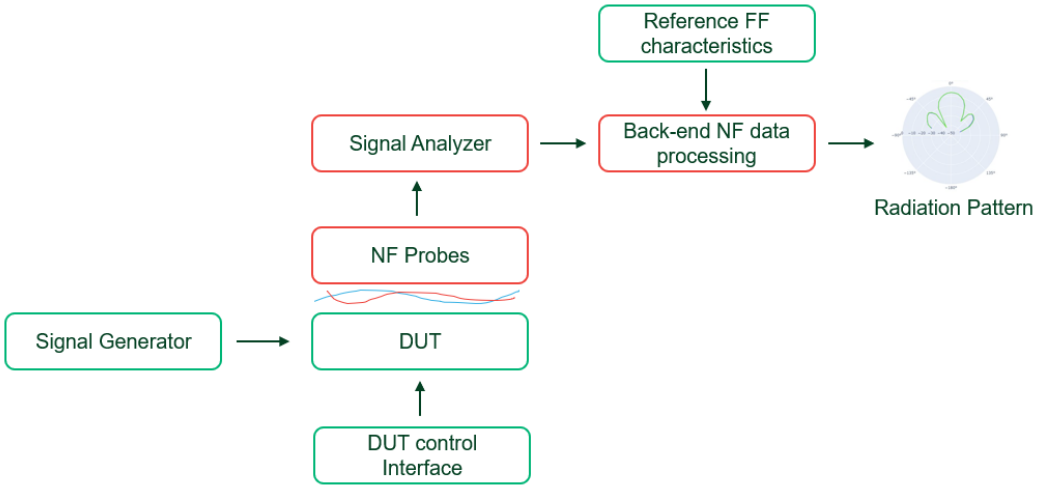

Figure 2.1: High level schema of the measurement system, in red the PAS high level blocks

It exploits a set of probes located in the NF, and from those measurements is able to reconstruct the far field characteristics of the DUT. Because of the NF approach, the PAS is much smaller than the conventional FF measurements system and cheaper as it eliminates the need of large chambers, mechanical movements and so reduces dramatically the measurement time. This method needs a calibration phase where the FF characteristics of a reference DUT are

known. This knowledge can be obtained by conventional measurements methods (e.g. anechoic chambers), as illustrated in the State of the Art and [17]. Then for the other DUTs of the same type to be tested, only NF measurements are needed. This features make this technology particularly suitable in production test scenarios, or similar applications that repeat measurements on a particular antenna design very often. At the current state different proof-of-concept PAS implementations for two active antennas exist. So far, for each DUT design a specific probe arrays was designed and for measuring DUT RX characteristics requires all probes to generate EM radiation simultaneously. This requires as many signal generators as the probes and the current system supports only up to 4 antenna elements. My work has the objective to make the technology more universal (i.e., one probe array design can cover multiple different DUT designs) and more scalable (i.e., lower the number of required Signal generators (SG) and Signal analyzers (SG)).

2.1 PAS PROOF-OF-CONCEPT REALIZATIONS

All the realized PASs use Vivaldi antenna probes that are planar, linearly polarized and broadband. The first distinction between PASs is their physical structure, (i.e., the probes alignment) to match the DUT's antennas location: each radiating elements has one probe on top. This makes the PAS a DUT-type dependent device. The DUTs I used to carry out the experiments are the Scarif and the NXP DUT, two mmWave prototype antennas.

SCARIF

The Scarif DUT is a phased array patch antenna developed by NI. In table (2.1) there are the specifications of the Scarif, while in (2.2) the antenna is shown. For each array element, it is possible to set 32 different amplitude configurations, which correspond to a step size of 1 dBm and 32 phases (phase step of 11.25°).

Parameter	Unit	Value
Frequency	GHz	26 up to 30
Polarization	-	Linear
Antenna Gain	dBi	>15
RF connector	-	SMA-K/2.92mm (female)
Number of radiating elements	-	16
Number of BF IC	-	4
TX Gain per IC	dB	26
RX Gain per IC	dB	28
Max RF input level per IC	dBm	0
Supply Voltage	V	5.0
Typical current (active)	A	1.5
Typical current (IDLE)	A	0.07

Table 2.1: Scarif specifications

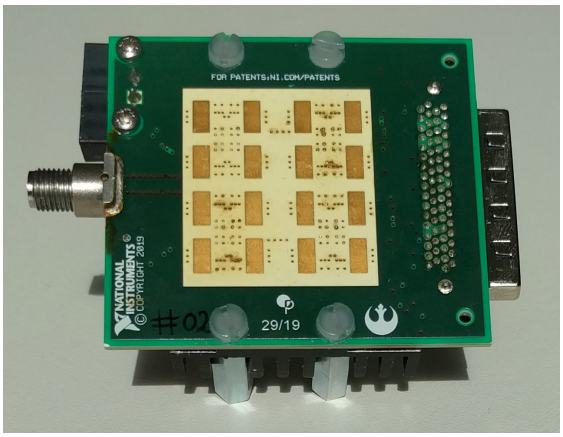

Figure 2.2: Scarif Antenna

The PAS that was built for this DUT is shown in figure 2.6a. One peculiarity of the Scarif antenna is that it is not possible to completely shut off individual elements, as they can be only set to their minimum emission power which is not negligible and must be taken into account in the reconstruction algorithm (this issue is due to the beam forming chip that was chosen in the antenna design).

NXP

The NXP antenna is a mmWave antenna designed by NXP Semiconductors, and handed over to NI. It is a 64 elements dual polarized antenna, with frequency ranging from 24.25 GHz to 27.5 GHz. In all the experiments, only one polarization was used. Since it has 8 bit registers for amplitude and phase setting (each), it is possible to set in total 256 gain and phase combinations per antenna element.

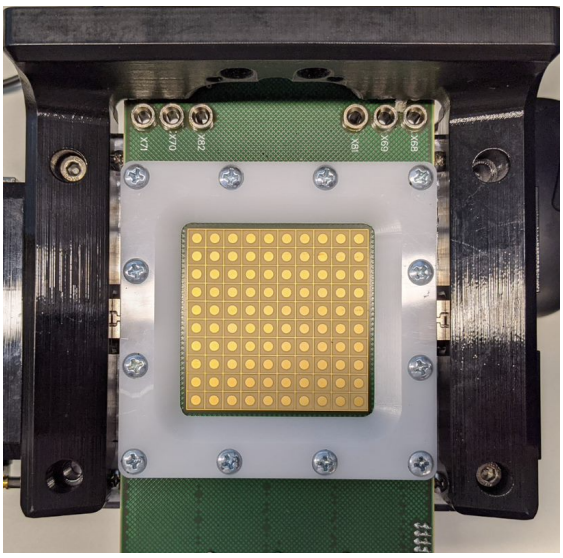

Figure 2.3: NXP Antenna: note that the outer elements are dummy, only the inner 8x8 elements are controlled by the IC circuits, the others are grounded

The second distinction between PASs is whether they are active or not. The difference between the two is that in the active PAS the final up/down conversion to/from the RF frequency (tens of GHz) is done at PAS level while the passive PAS needs an external device to do that. In figure 2.4 a block diagram of the passive PAS structure in which a DUT with 4 antennas are used. In the passive case, if we have N antennas to be tested, then we need N high frequency cables that connect the probes outputs to the external up/down converter (mmWave Radio Head). Moreover, the read of the probes is done sequentially by means of a switching matrix. Assuming the signal to be periodic and stationary, the sequential probe read is done by a single signal analyzer, prior a synchronization with the signal generator in order to identify the beginning of a period. Note that at NI the SG and SA are incorporated in a single module named VST (Vector Signal Transceiver).

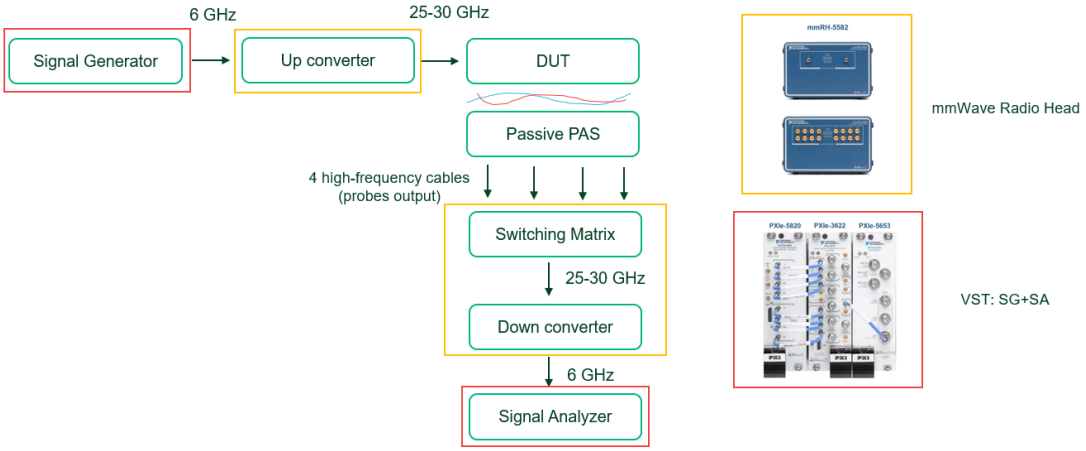

Figure 2.4: Passive PAS block diagram

The active PAS, whose block diagram is in figure 2.5, exploits a number of VSTs equal to the number of DUT antennas. This choice is mainly due to the fact that in order to test the DUT receiving properties via PAS we need to be able to drive simultaneously the probes (more on this in the next chapters). Since the final up/down conversion is done at PAS level, we need also N up/down converters. This is a problem for the scalability of the technology for DUTs with high number of antennas. We can use the active PAS for both RX and TX testing, in the latter it leads to more stable results compared to the passive one as we don't need high frequency cabling, but at the same time we are limited by the number of channels available. At the current stage a 4 channels active PAS is available, allowing to test the Scarif DUT with not more than 4 active antennas.

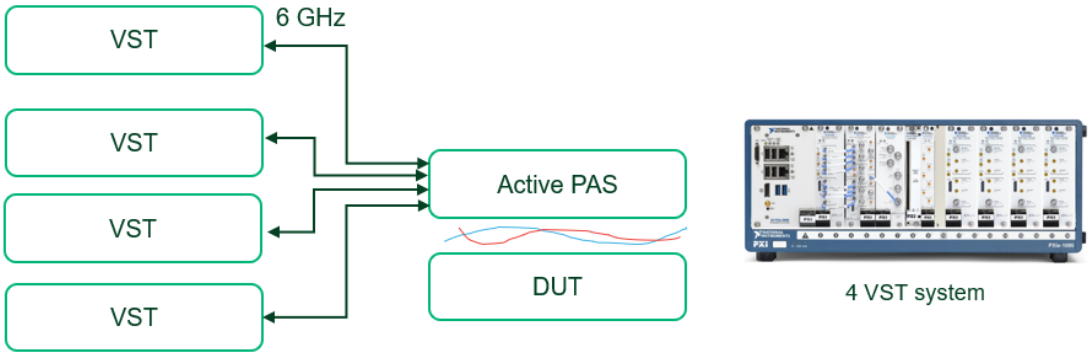

Figure 2.5: Active PAS block diagram

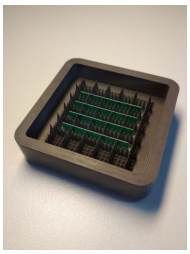

(a) Scarif passive PAS

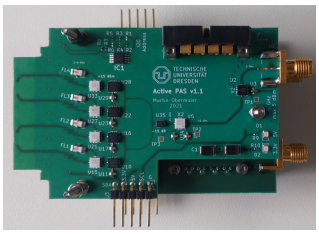

(b) Scarif Active PAS

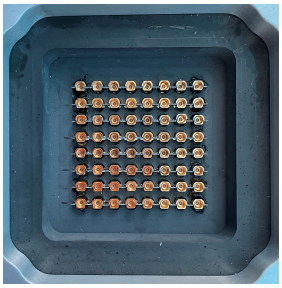

(c) NXP Passive PAS (upside)

Figure 2.6: Probe Arrays

2.2 Model for DUT Transmit Measurements

In this section a theoretical justification [2] of the model on which both TX and RX NF to FF reconstruction algorithms are based is presented. Starting from the IEEE definition of directivity $D(\theta,\phi) = \frac{4\pi U(\theta,\phi)}{P_{rad}}$ and radiated power per unit solid angle $U(\theta,\phi) = \frac{|\boldsymbol{E}(r,\theta,\phi)|^2 r^2}{2\eta}$, we can write the squared peak amplitude of the electrical field produced by a generic antenna n, that we assume to be part of an antenna array of N elements, in a position (r,θ,ϕ) in the far field as:

$$|\boldsymbol{E}_n(r,\theta,\phi)|^2 = \frac{\eta P_{rad,n} D_n(\theta,\phi)}{2\pi d_n(r,\theta,\phi)^2} \tag{2.1}$$

where η is the intrinsic impedance of free space (approximately 377Ω), P_{rad} is the total radiated power of the n-th antenna and $d_n(r,\theta,\phi)$ is the distance that the wave travels from that antenna to the given position (r,θ,ϕ). The coordinate system is the usual spherical one, depicted in figure 2.7, where the origin is the center of the array.

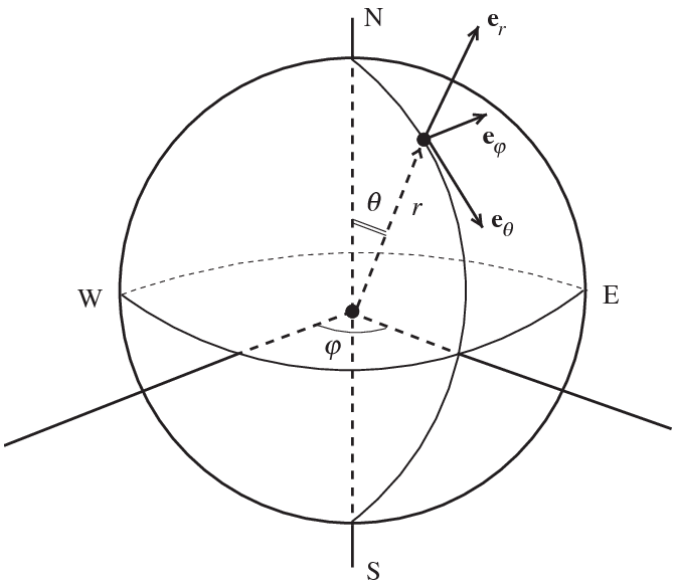

Figure 2.7: Spherical coordinate system, picture from [3]

In our scenario we have an array of N emitting antennas, each one with its specific configuration settings w_n, i.e. amplitude and phase settings. For notation simplicity, we assume the power of the antenna to be concentrated in only one polarization component (the extension to dual-polarized antennas is straightforward). Therefore we can use (2.1) and write the total electric field in

the FF as:

$$\begin{aligned} E(r,\theta,\phi) &= \sum_{n=1}^{N} |E_n(r,\theta,\phi)| e^{-j\beta_n(w_n)} e^{-jkd_n(r,\theta,\phi)} \\ &= \sum_{n=1}^{N} \sqrt{\frac{\eta P_{rad,n}(w_n) D_n(\theta,\phi)}{2\pi d_n(r,\theta,\phi)^2}} e^{-j\beta_n(w_n)} e^{-jkd_n(r,\theta,\phi)} \end{aligned} \tag{2.2}$$

In the above equation we have:

- $\beta_n(w_n)$ is the phase due to the setting (magnitude and phase) for the n-th array element w_n.
- $k = 2\pi/\lambda$ is the usual wave number in free space, to account for the phase acquired by the wave travel.

Note that in (2.2) we assumed that each antenna's radiated power and phase depend exclusively on its own configuration setting w_n. In fact, in the most general case, the actual phase and radiated power of each antenna can be somehow correlated to the settings of the other elements, due to some unwanted couplings between the elements usually modeled via scattering matrices. The parameters would then be rewritten as $\beta_n(\boldsymbol{w})$ and $P_{rad,n}(\boldsymbol{w})$ where $\boldsymbol{w}$ is a vector containing the settings of all the elements. Equation 2.2 can be further simplified by normalizing the electrical field by the observer distance r. We do this because of comparability of results across different test setups with different measurement distances. We can also approximate $d_n(r,\theta,\phi) \simeq r$. Note that for the distance term this approximation is appropriate, while for the phase term it is not as even slight differences in the path can have a significant impact on the resulting wave phase, especially at high frequencies. We can rewrite then the phase term as $d_n(r,\theta,\phi) = r + \Delta d_n(\theta,\phi)$ where $\Delta d_n(\theta,\phi)$ is the difference between the n_{th} antenna path length and the one with respect to the reference point of the array system (i.e., the origin of our spherical coordinate system). Said so, equation 2.2 becomes:

$$\begin{aligned} E(\theta,\phi) &= rE(r,\theta,\phi) \\ &= \sum_{n=1}^{N} \sqrt{\frac{\eta P_{rad,n}(w_n) D_n(\theta,\phi)}{2\pi}} \frac{r}{d_n(r,\theta,\phi)} e^{-j\beta_n(w_n)} e^{-jkd_n(r,\theta,\phi)} \\ &\simeq \sum_{n=1}^{N} \sqrt{\frac{\eta P_{rad,n}(w_n) D_n(\theta,\phi)}{2\pi}} e^{-j\beta_n(w_n)} e^{-jk\Delta d_n(\theta,\phi)} e^{-jkr} \end{aligned} \tag{2.3}$$

The term e^{-jkr} can be neglected as it is the same for all the antennas elements, and it does not bring any useful information but a common phase offset. We can now group the elements in equation 2.3 defining two new quantities as follows:

- $c_n(w_n) = \sqrt{\frac{\eta P_{rad,n}(w_n)}{2\pi}} e^{-j\beta_n(w_n)}$ can be seen as a weighting factor that the n-th antenna has in the FF. We can notice that this quantity depends only on the settings w_n and it is position independent.
- $f_n(\theta, \phi) := \sqrt{D_n(\theta, \phi)} e^{-jk\Delta d_n(\theta,\phi)}$ can be seen as a radiation pattern (magnitude and phase), or *base function*, that accounts for the intrinsic antenna characteristics and position.

Doing so the equation (2.3) can be rewritten as

$$E(\theta, \phi) = \sum_{n=1}^{N} c_n(w_n) f_n(\theta, \phi) \tag{2.4}$$

i.e., a sum of N base functions scaled by their respective weighting factors.

2.2.1 How the PAS works

Since Maxwell equations are linear, the core assumption onto which the PAS technology is based on is that we can impose *linearity* between near field and far field measurements. We can split the whole PAS reconstruction procedure in three high level phases:

1. Calibration
2. NF to FF mapping
3. Single element superposition

that are summarized and depicted below.

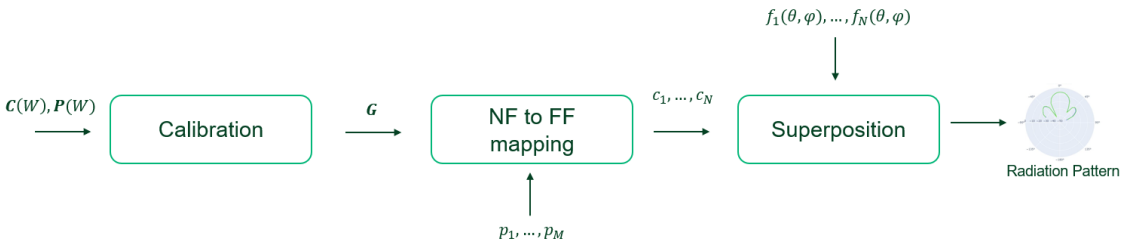

Figure 2.8: TX reconstruction algorithm baseline schema

Calibration Phase

In our case, the linearity is exploited in imposing the relation (2.5):

$$\boldsymbol{c}(\boldsymbol{w}) = \boldsymbol{G} \cdot \boldsymbol{p}(\boldsymbol{w}) \tag{2.5}$$

where $\boldsymbol{c}(\boldsymbol{w}) = [c_1(\boldsymbol{w}), ..., c_N(\boldsymbol{w})]$ is a vector containing the N antennas weighting factors, while $\boldsymbol{p}(\boldsymbol{w}) = [p_1(\boldsymbol{w}), ..., p_M(\boldsymbol{w})]$ contains the NF measurements. M refers to the number of probes elements that are exploited to carry out parallel measurements in the Near Field.
The calibration phase has two objectives:

1. Estimation of the single element FF patterns $f_n(\theta, \phi)$
2. Estimation of the reconstruction matrix $\boldsymbol{G}$

In order to estimate $\boldsymbol{G}$ a set of NF measurements $\boldsymbol{p}(\boldsymbol{w})$ and a known set of weighting factors $\boldsymbol{c}(\boldsymbol{w})$ (that are estimated via FF measurements) are used. We can perform multiple NF and FF measurements with different configuration settings $\boldsymbol{w}$, and so we measure different realizations of $\boldsymbol{p}(\boldsymbol{w})$ and $\boldsymbol{c}(\boldsymbol{w})$. Ultimately, we can perform a Least Square optimization using (2.5) and find $\boldsymbol{G}$. To do that, we can define the matrices $\boldsymbol{C} = [\boldsymbol{c}(\boldsymbol{w}_1), ..., \boldsymbol{c}(\boldsymbol{w}_K)]$ and $\boldsymbol{P} = [\boldsymbol{p}(\boldsymbol{w}_1), ..., \boldsymbol{p}(\boldsymbol{w}_{K)}]$ that contain the measured FF weighting factors and NF indications at different configuration settings $\boldsymbol{w}_i$, respectively. K is the number of configurations we decide to use. If we did not have noise, assuming the same number N of DUT and PAS antennas, then we would need exactly N different settings in order to estimate $\boldsymbol{G}$. Moreover, from an algebraic point of view, we can see immediately that we need $M \geq N$ probes to correctly reconstruct the FF pattern of the array. Note that it is crucial that the settings used for the far field and near field measurements are the same: $\boldsymbol{p}(\boldsymbol{w}_i)$ and $\boldsymbol{c}(w_i)$ are found by feeding the DUT with the same settings $\boldsymbol{w}_i$. We can now find the calibration matrix $\boldsymbol{G}$ by solving:

$$\boldsymbol{G} = argmin_{G'} ||\boldsymbol{C} - \boldsymbol{G}'\boldsymbol{P}||^2 \tag{2.6}$$

which has as solution:

$$\boldsymbol{G} = \boldsymbol{C}\boldsymbol{P}^{\dagger} \tag{2.7}$$

where $\boldsymbol{P}^{\dagger}$ is the pseudo inverse of $\mathbf{P}$ defined as

$$\boldsymbol{P}^{\dagger} = \mathbf{P}^H(\mathbf{P}\mathbf{P}^H)^{-1} \tag{2.8}$$

where H is the Hermitian operator (transpose-conjugate). Note that the calibration needs to carried out only *once*. The open point is how in practice measure the weighting factors and the single element patterns. In few words, the current implementation doesn't estimate exactly those parameters, as we have access only to the received electrical field which always contains the effect of both settings and spatial information. In Appendix A there is the explanation on how to combine these pseudo-estimations in order to correctly reconstruct the FF radiation pattern. Moreover, it is also explained how to handle the interference when dealing with not ideal DUTs.

NF to FF mapping

Once the matrix $\boldsymbol{G}$ is known, we can find the realized weighting factors for a certain beam configuration only via NF measurements, i.e. find $\boldsymbol{c}(\boldsymbol{w})$ by a single parallel reading of $\boldsymbol{p}(\boldsymbol{w})$ in the NF. Thus, after the calibration, we only need NF measurements to reconstruct the FF patterns.

Single Element Superposition

We can finally combine the weighting factors and the single element patterns and reconstruct the radiation pattern of the DUT via superposition (2.4).

2.2.2 Results

This method was first published in [11], and in Fig. 2.9 a beam reconstruction is shown. Note that in order to evaluate the reconstruction performance a visual approach on the Azimuth and Elevation cuts is used. One could in principle define some metrics of evaluation (e.g., boresight error, side-lobe-level,...) still this pretty much depends on the customer needs and situations.

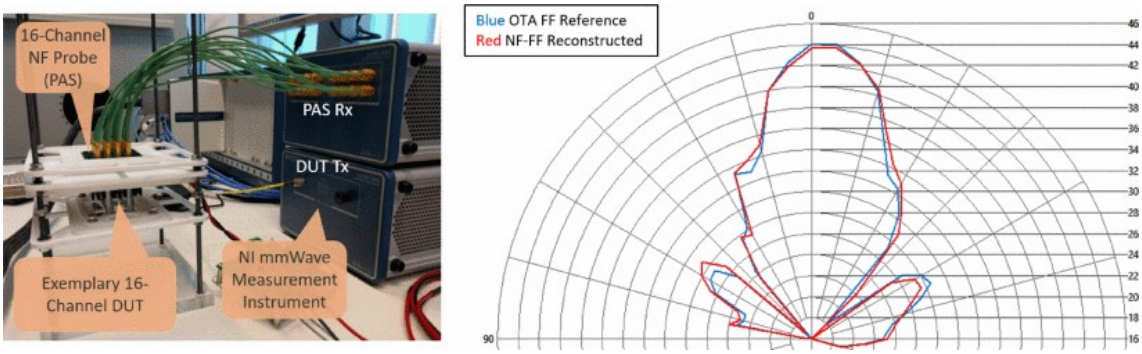

Figure 2.9: Reconstruction performance: Scarif DUT

As explained in [11], the minimum distance between PAS and DUT is of few mm, which means that the PAS is actually positioned in the DUT reactive field. According to [2], to be in the NF of a DUT with aperture size D at frequency $f = \frac{c}{\lambda}$ a distance of r_{NF} is needed:

$$r_{NF} = 0.62\sqrt{D^3/\lambda} \tag{2.9}$$

In our case, at 28 GHz this translates into a distance of $r_{NF} \approx 6.7cm$. Still, the PAS structure (in particular the absorbers) is designed such that it operates in the single element NF, allowing a more compact system without the risk of having a loading effect on the DUT. Note that the impact that the distance/structure of PAS has on the reconstruction performances is one of the internship studies (see the chapter on the Generalized PAS experiment). Lastly, in figure 2.10 a reconstruction at 25.875 GHz with the NXP DUT is reported.

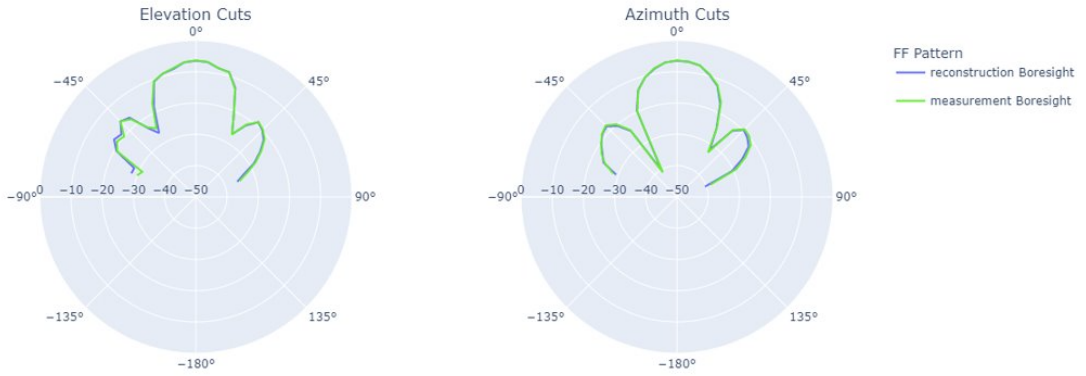

Figure 2.10: Reconstruction performance: NXP DUT

2.3 DUT RX CHARACTERIZATION

Analogously to the transmitting properties, also the receiving properties of the DUT need to be characterized. One could in principle invoke the reciprocity conditions, and state that transmitting and receiving properties are the same. This is true if we were dealing with a fully symmetrical system, but in practice this is not the case. Often, the transmitting and receiving beamforming circuitry are not the same (see Fig.2.11), with different amplifiers, phase shifters and attenuations. The whole system is then no longer symmetrical, and reciprocity does not hold anymore. In this section, we first derive a FF measurement model with which a characterization of the DUT RX properties is done via classical methods. Then a NF model derivation is explained, where now is the PAS that generate the EM signal that impacts the DUT in the NF. Our aim is again to replace a FF measurement setup by our NF PAS approach but still be able to reconstruct the DUT Rx response to plane wave excitation from sources at arbitrary directions in the FF. We first model the measurement of the DUT Rx sensitivity pattern with the stimulus source moved across directions in the FF, then a model for the NF using a fixed position PAS is proposed. Ultimately, an algorithm that reproduces the effect of a plane wave coming from the FF but using the PAS in the NF is presented.

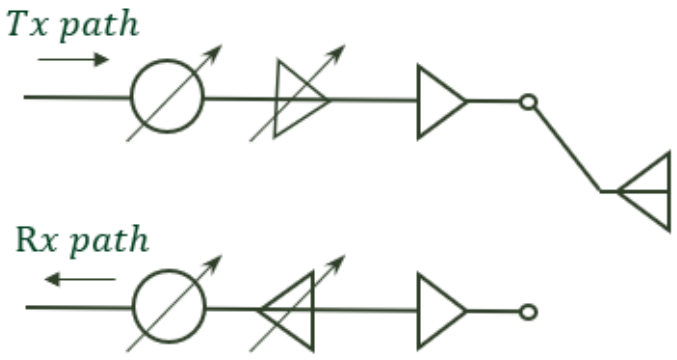

Figure 2.11: High level schema of a DUT's antenna in TX mode

2.3.1 FF Model Derivation

The FF reference scenario is shown in figure 2.12, and there we have:

- $a_{FF}(\boldsymbol{w}, \theta_m, \phi_m)$ is the DUT output if an EM wave coming from direction (θ_m, ϕ_m) impacts the DUT and where the DUT Rx beamformer settings are $\boldsymbol{w}$.
- b_m is the source input signal.
- $\boldsymbol{s}(\theta_m, \phi_m) = [s_1(\theta_m, \phi_m), ..., s_N(\theta_m, \phi_m)]^T$ are the output of the DUT antennas when an EM wave coming from direction (θ_m, ϕ_m) impacts the DUT.

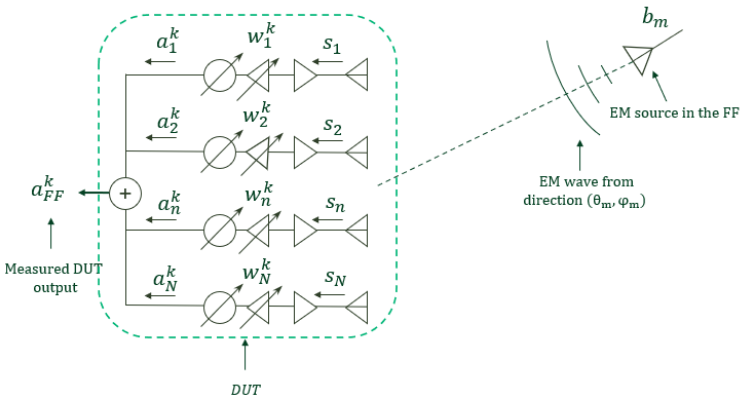

Figure 2.12: DUT Rx response to a plane wave excitation from a FF source at one direction

The problem with this setup is that to test the DUT we would need a source in the far field, which would require an anechoic chamber and a lot of time. The core idea is then replacing the FF source with the PAS, positioned in a fixed position in the DUT near field, that would emulate the behavior of a plane wave coming from the far field with the same direction (θ_m, ϕ_m). We can write the DUT output as:

$$\begin{aligned} a_{FF}(\boldsymbol{w}, \theta_m, \phi_m) &= \sum_{n=1}^{N} c_n(w_n) f_{FF,n}(\theta_m, \phi_m) b_m \\ &= \boldsymbol{c}(\boldsymbol{w})^T \boldsymbol{s}(\theta_m, \phi_m) \end{aligned} \tag{2.10}$$

where

- $\boldsymbol{c}(\boldsymbol{w})^T$ is the N-elements vector containing the weighting factors that each antenna element has in the output signal $a_{FF}(\boldsymbol{w}, \theta_m, \phi_m)$, which depends on the settings of the individual antenna.

- $f_{FF,n}(\theta_m, \phi_m)$ can be interpreted as the single element RX pattern *base function*. It takes into account the antenna's effective length, polarization and impedance matching. This coefficient is used basically to couple the signal coming from the TX antenna to the DUT antenna's output port, i.e. $s_n(\theta_m, \phi_m) = f_{FF,n}(\theta_m, \phi_m) b_m$.

2.3.2 NF Model Derivation

We can now model the DUT in RX mode response when the signal is generated by a PAS (that now is *active*) placed in the near field. The system is depicted in figure 2.13. The output signal can be written in a similar way as the FF case,

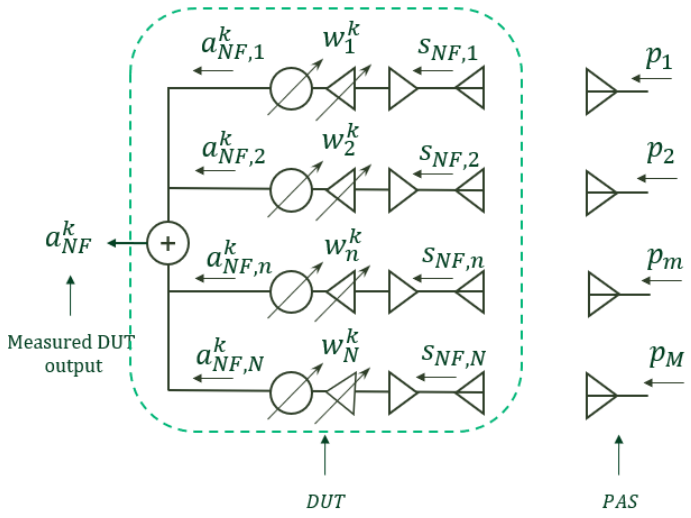

Figure 2.13: DUT response to the NF generated stimuli

i.e.:

$$\begin{aligned} a_{NF}(\boldsymbol{w}) &= \sum_{n=1}^{N} c_n(w_n) s_{NF,n} \\ &= \sum_{n=1}^{N} \sum_{m=1}^{M} c_n(w_n) f_{NF,n,m} p_m \\ &= \boldsymbol{c}(\boldsymbol{w})^T (\boldsymbol{F}_{NF} \cdot \boldsymbol{p}) = \boldsymbol{c}(\boldsymbol{w})^T \boldsymbol{s}_{NF}(\boldsymbol{p}) \end{aligned} \tag{2.11}$$

In the above equation:

- $\boldsymbol{c}(\boldsymbol{w})^T$ is the same as 2.3.1, as it is determined by the beam forming circuits.
- $\boldsymbol{F}_{NF}$ is the coupling matrix between the PAS inputs $\boldsymbol{p}$ and the DUT antennas outputs $\boldsymbol{s}_{NF}$, i.e. $\boldsymbol{s}_{NF}(\boldsymbol{p}) = \boldsymbol{F}_{NF} \cdot \boldsymbol{p}$. It has dimension NxM where M is the number of PAS antennas, and the element $\boldsymbol{F}_{NF,n,m} = f_{NF,n,m}$ is the coupling coefficient between the PAS antenna m and the DUT antenna n.

2.4 Weighting factors, single element patterns and coupling matrix estimation

$c_n(w_n)$ and $f_{FF,n}(\theta_m, \phi_m)$ estimation

In order to estimate these coefficients, an antenna positioned in the far field is needed. Still, as it will be shown in the next sections, these measurements are then exploited in a calibration phase, very much like the TX case, and so it must be done only once. If we shut down all the elements but the one we want to estimate the coefficients, let us say element n, equation 2.10 becomes:

$$a_{FF}(\boldsymbol{w}, \theta_m, \phi_m) = c_n(w_n) f_{FF,n}(\theta_m, \phi_m) b_m$$

Note that in the definition (2.10) $\boldsymbol{w}$ refers to an arbitrary combination of settings, one for each element. Here, $\boldsymbol{w}$ is such that $c_n(w_n)$ is non-zero only for DUT element n. We can then estimate the weighting factors for the antenna n as:

$$\tilde{c}_n(w_n) = \frac{a_{FF}(\boldsymbol{w_n}, \theta_0, \phi_0)}{a_{FF}(\boldsymbol{w_0}, \theta_0, \phi_0)} = \frac{c_n(w_n)}{c_n(w_0)} \tag{2.12}$$

where $\boldsymbol{w_n} = [0, ..., w_n, ..., 0]$ and $\boldsymbol{w_0} = [0, ..., w_0, ..., 0]$ is the *reference setting*, where all the element are turned off but the element n that is set to w_0. The direction (θ_0, ϕ_0) can be arbitrary, but can be chosen such that to maximize the SNR. These coefficients are an intrinsic property of the DUT, depend only on the settings ($\boldsymbol{w_0}$ and $\boldsymbol{w_n}$) and thus are independent of the incoming wave. Note that in (2.12) both numerator and denomination are measured with the same source excitation b_m. We can estimate the single element RX pattern by measuring the DUT output:

$$\tilde{f}_{FF,n}(\theta_m, \phi_m) = \frac{a_{FF}(\boldsymbol{w_0}, \theta_m, \phi_m)}{b_m} = \frac{c_n(w_0) f_{FF,n}(\theta_m, \phi_m)}{b_m} \tag{2.13}$$

Note that once these coefficients are known, an estimation of the vector $\boldsymbol{s}(\theta_m, \phi_m)$ is fully determined. In fact:

$$\tilde{s}_n(\theta_m, \phi_m) = \tilde{f}_{FF,n}(\theta_m, \phi_m) b_m = c_n(w_0) s_n(\theta_m, \phi_m) = a_{FF}(\boldsymbol{w_0}, \theta_m, \phi_m) \quad (2.14)$$

We can write the estimated $\tilde{\boldsymbol{s}}(\theta_m, \phi_m)$ in matrix form as:

$$\tilde{\boldsymbol{s}}(\theta_m, \phi_m) = \boldsymbol{C}(\boldsymbol{w}_0) \boldsymbol{s}(\theta_m, \phi_m) \quad (2.15)$$

where the matrix $\boldsymbol{C}(\boldsymbol{w}_0)$ is a NxN diagonal matrix in which the elements $\boldsymbol{C_{n,n}} = c_n(w_0)$. As for the TX case, these estimations of the single element patterns depend on the reference setting. It is crucial that both the single element patterns and the weighting factors are measured with the same reference setting, only in this way we can combine them to obtain the correct RX pattern.

Coupling matrix estimation

The missing piece for the system to work is how to determine the coupling matrix $\boldsymbol{F}_{NF}$. Recalling equation (2.11), we can perform K different measurements, each one of them with different settings $\boldsymbol{w}$, and record the outputs into the vector $\boldsymbol{a}_{NF}(\boldsymbol{W})$. For each of these settings, we can record also the corresponding weighting vector $\boldsymbol{c}(\boldsymbol{w})$, and construct the weighting matrix $\boldsymbol{C}(\boldsymbol{W})$ whose columns are the weighting vectors. If we also require that only one PAS antenna is transmitting at a time we can rewrite equation (2.11) as:

$$\boldsymbol{a}_{NF,m}(\boldsymbol{W}) = \boldsymbol{C}(\boldsymbol{W}) \boldsymbol{f}_{NF,m} p_m \quad (2.16)$$

where $\boldsymbol{f}_{NF,m}$ is the m_{th} column of the coupling matrix $\boldsymbol{F}_{NF}$ and p_m is the input of the only PAS antenna active. The dimensions of $\boldsymbol{a}_{NF}(\boldsymbol{W})$ and $\boldsymbol{C}(\boldsymbol{W})$ are Kx1 and KxN with $K > N$, respectively. We can now invert equation 2.16 and find one column of $\boldsymbol{F}_{NF}$ as:

$$\boldsymbol{f}_{NF,m} = \boldsymbol{C}(\boldsymbol{W})^{\dagger} \boldsymbol{a}_{NF,m}(\boldsymbol{W}) / p_m \quad (2.17)$$

We can repeat this procedure for all the PAS antennas (M times), and so estimate $\boldsymbol{F}_{NF}$.

In practice, we do not have access neither to the the single element patterns nor weighting factors. We can measure only their estimates, i.e. $\tilde{c}_n(w_n)$ and

$\tilde{\boldsymbol{s}}(\theta_m, \phi_m)$. Consequently we have access only to the matrix:

$$\tilde{\boldsymbol{C}}(\boldsymbol{W}) = \boldsymbol{C}^{-1}(\boldsymbol{w}_0) \cdot \boldsymbol{C}(\boldsymbol{W}) \tag{2.18}$$

that is a scaled version of the true weighting factor matrix $\boldsymbol{C}(\boldsymbol{W})$. Then if we use the weighting vector estimations in (2.17) we will end up with a scaled version of the true coupling matrix:

$$\tilde{\boldsymbol{F}}_{NF} = \boldsymbol{C}(\boldsymbol{w}_0) \cdot \boldsymbol{F}_{NF} \tag{2.19}$$

There are two algorithms that exploit the models just presented to perform DUT RX testing, and in both of them only the estimates of the true quantities are used. Still, we can use these estimations as if they were the true values since both the weighting factors and single element patterns were measured with the same reference setting $\boldsymbol{w}_0$. This claim will be demonstrated for both the algorithms, in the next section the first one is presented.

2.5 Sparse point RX reconstruction algorithm

This is the first reconstruction algorithm used for RX characterizations. The working principle is based on emulating the impact that a FF plane wave has on the DUT via NF excitations. In chapter 4, a novel method is proposed.
If we compare equation (2.10) and (2.11) we can notice that we can reproduce the effects that a far field wave has on the DUT with the PAS. It is sufficient to impose the output of the DUT antennas of the two cases to be the same:

$$\boldsymbol{s}_{NF}(\boldsymbol{p}) = \boldsymbol{s}(\theta_m, \phi_m) \tag{2.20}$$

Recall that the vectors $\boldsymbol{s}(\theta_m, \phi_m)$, i.e. the DUT antennas outputs when a FF wave coming from direction (θ_m, ϕ_m) impinges on it, are known after the estimation phase in Section 2.4. If we know the coupling matrix $\boldsymbol{F}_{NF}$, we find the excitation values for the PAS using the inverse matrix $\boldsymbol{F}_{NF}^{-1}$:

$$\boldsymbol{s}_{NF}(\boldsymbol{p}) = \boldsymbol{F}_{NF} \cdot \boldsymbol{p} = \boldsymbol{s}(\theta_m, \phi_m) \Rightarrow \boldsymbol{p} = \boldsymbol{F}_{NF}^{-1} \boldsymbol{s}(\theta_m, \phi_m) \tag{2.21}$$

If we now use the estimations of the coupling matrix and single element patterns from equations (2.19) and (2.15) in eq.(2.21) in place of the true values, we will

end up with:

$$\begin{aligned}\tilde{\boldsymbol{p}} &= \tilde{\boldsymbol{F}}_{NF}^{-1}\tilde{\boldsymbol{s}}(\theta_m, \phi_m) \\ &= \boldsymbol{F}_{NF}^{-1}\boldsymbol{C}^{-1}(\boldsymbol{w}_0) \cdot \boldsymbol{C}(\boldsymbol{w}_0)\boldsymbol{s}(\theta_m, \phi_m) = \boldsymbol{p}\end{aligned} \tag{2.22}$$

i.e., using the "true" values and their estimations lead to the *same* stimuli. This means that instead of using $\boldsymbol{F}_{NF}$ and $\boldsymbol{s}(\theta_m, \phi_m)$ (that we cannot access) we can use their estimations (that can be measured) in determining the desired stimuli $\boldsymbol{p}$.

In Figure 2.14 the 4-modules VST used to drive the 4-elements active PAS is shown, while in Fig. 2.15 we show the whole system. Measurements were performed on the Scarif antenna with four of its elements being active. The interference compensation was performed analogously to the transmitting case, i.e. setting the dummy elements to a known state and subtracting their effect from the calibration data. In Fig. 2.16 different reconstructions at 28 GHz with different beams is shown. The reference pattern are FF measurements carried in the chamber. We can notice that the reconstructions are little worse than the TX case with considerable deviations from the reference patterns. In Fig. 2.18 we have the reconstructions at different frequencies while on Fig. 2.17 an evaluation on the repeatibility of the measurements is asserted.

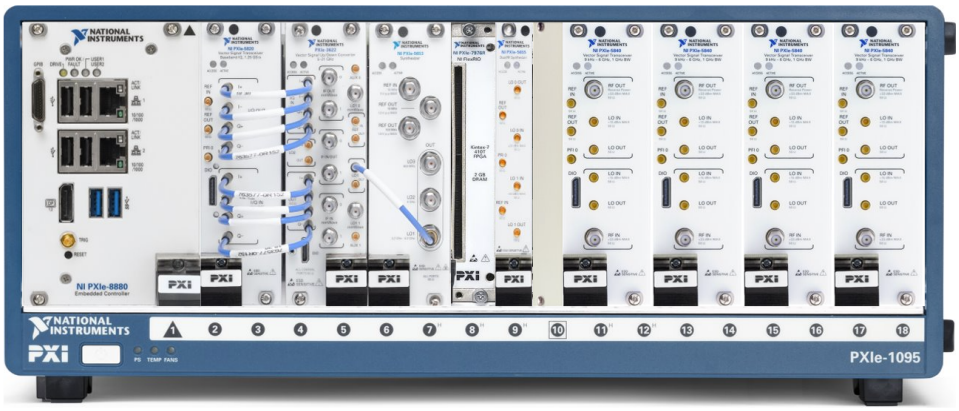

Figure 2.14: 4-modules VST

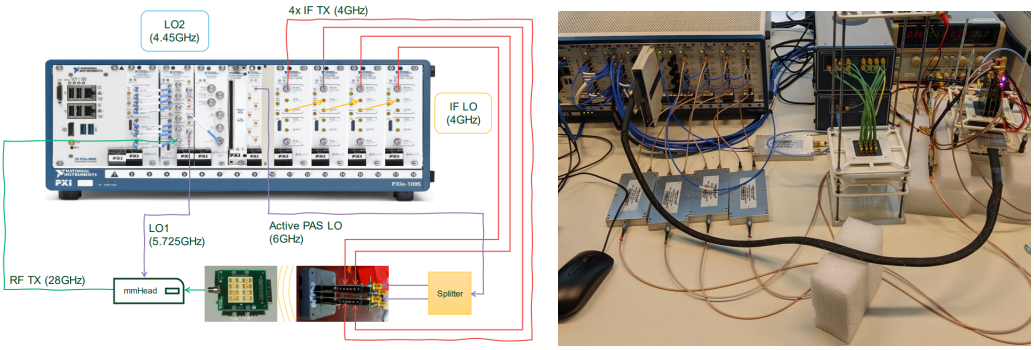

(a) Block diagram (b) NF system

Figure 2.15: System to test the DUT in RX mode in the NF

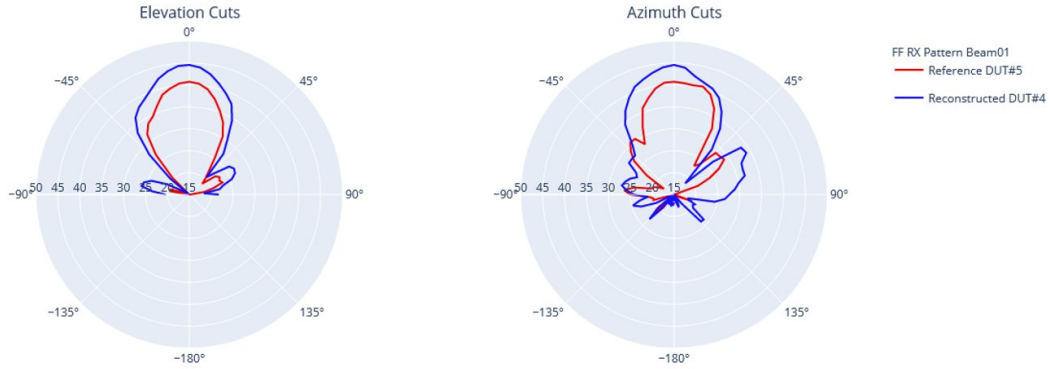

(a) Beam 1

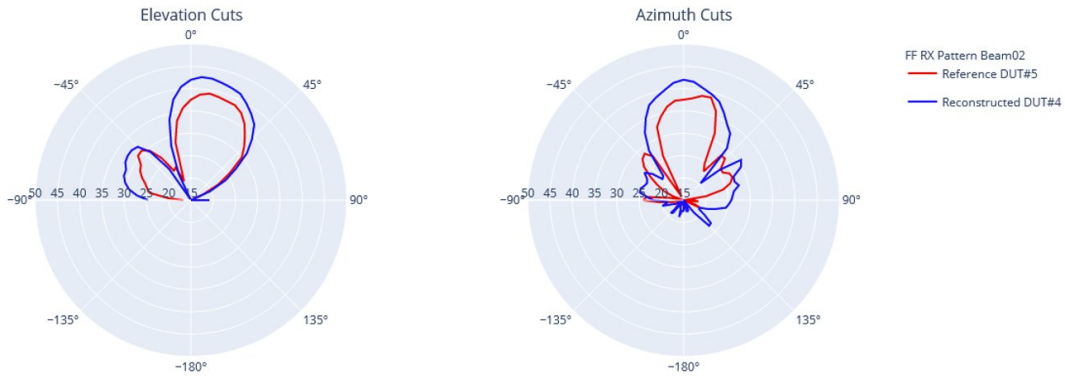

(b) Beam 2

Figure 2.16: RX reconstructions at 28 GHz

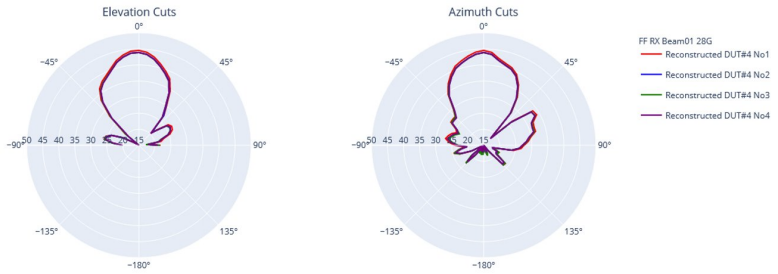

Figure 2.17: Beam 1 at 28 GHz - repeatibility of the measurements

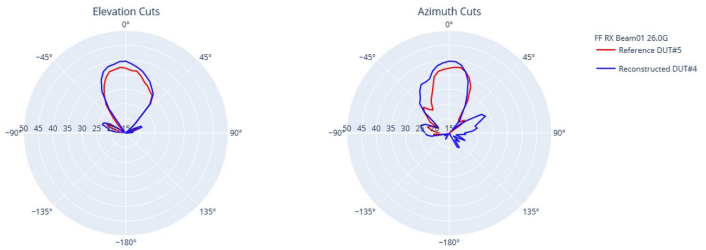

(a) 26 GHz

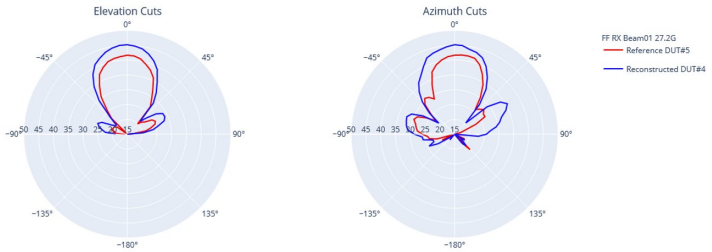

(b) 27.2 GHz

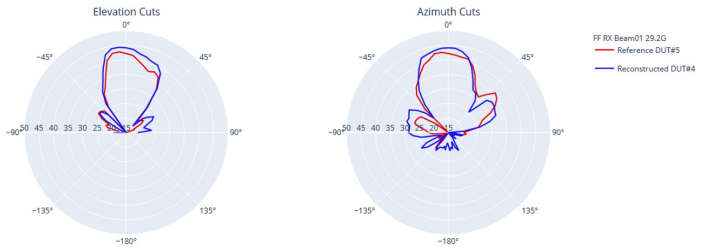

(c) 29.2 GHz

Figure 2.18: RX reconstructions of Beam 1 at different frequencies

The main shortcoming of this approach is for sure the cost of the system and

its scalability. In fact in order to drive the PAS to obtain the desired situation in the NF we need to have at least as many probes as the number of DUT antennas, and each probe needs to be driven by its own VST. In the chapter "Beam formed PAS" a possible method to tackle this issue is presented. Another shortcoming of this approach is that, after the calibration, we need to perform one NF measurement for every point in the pattern we are interested in. This might not be a problem when only a few specific points of the pattern are of interest, but if denser evaluations are needed then this method might take excessively long times. A way to tackle this problem is presented in the Chapter 4. Lastly, we might be limited by the dynamic range of the VST and so in practice the output signals required in (2.21) might not be feasible. Note that the limitation is due to the amplitude of the required stimuli, and to cope with that in the current implementation every stimuli's amplitude is digitally normalized to the maximum that the SG can support, and this scaling factors are recorded. Then, the output produced by each of the stimuli is multiplied with the inverse of the scaling factor of the stimuli that produced it. Ultimately, all the scaled responses are summed up.

2.6 Conclusions

Overall the PAS seems to be a promising technology, but more work needs to be done. For what concerns the reconstruction performances in the TX case we are able to obtain better results compared to the RX case. To test the DUT in TX case a generalization of the current technology to cope with variable sizes DUT is needed, while for the RX case we need a way to reduce the number of channels required by the system to operate and the measurement time in the case of dense pattern points evaluation. All these problems will be tackled in the next chapters, which are my contribution to the development of the technology.

3

Generalized PAS

One of the problems of the current PAS technology is the fact that, so far, each DUT was tested with a PAS specifically designed for it. Each PAS system in fact has been designed such that each probe position would match exactly the position of the DUT antennas, i.e. to be on top of that. In the best case scenario, from the technology usability viewpoint, the PAS should be a surface of probes independent from the DUTs sizes so that the same PAS can be used for different DUTs. The goal of the Generalized PAS experiment is to test how much the PAS system is sensible to the DUT structure. Moreover, we will also study what happens when using a number of probes greater than the number of emitting antennas: We recall that in principle in order to capture all the degrees of freedom of the DUT array we need to use at least the same number of probes as the number of emitting antennas. Theoretically, using more probes would only improve the reconstruction as more power gets collected. To carry out the experiment the NXP and Scarif DUTs are used as well as their PAS, we can divide the experiment in 2 sections:

- Use the NXP PAS to measure the Scarif DUT
- Use the Scarif PAS to measure the NXP DUT

and for each section, different sets of probes were used.

3.1 NXP PAS and Scarif DUT

In this experiment, the Scarif DUT is measured by means of the NXP PAS. We recall that in the Scarif the elements cannot be turned off completely, and so an interference compensation is needed (see appendix A). The system settings are the following:

- SG output power: -3 dBm
- SA reference level: -13 dBm
- Frequency: 28 GHz
- Number of emitting antennas: 4
- Active elements configuration: span on 3 amplitudes and 32 phases each
- Non-mutable (interfering) elements configuration: fixed amplitude and phase

A reference scheme is shown in figure 3.1. Note that in the scheme the relative position between DUT antennas and PAS probes is not precise, as the structure of the PAS does not match the DUT structure: the Scarif was positioned such that the emitting antennas are somehow in the center of the PAS structure, and so "aligned" in some sense with probes 6,7,10,11. The experiment consists

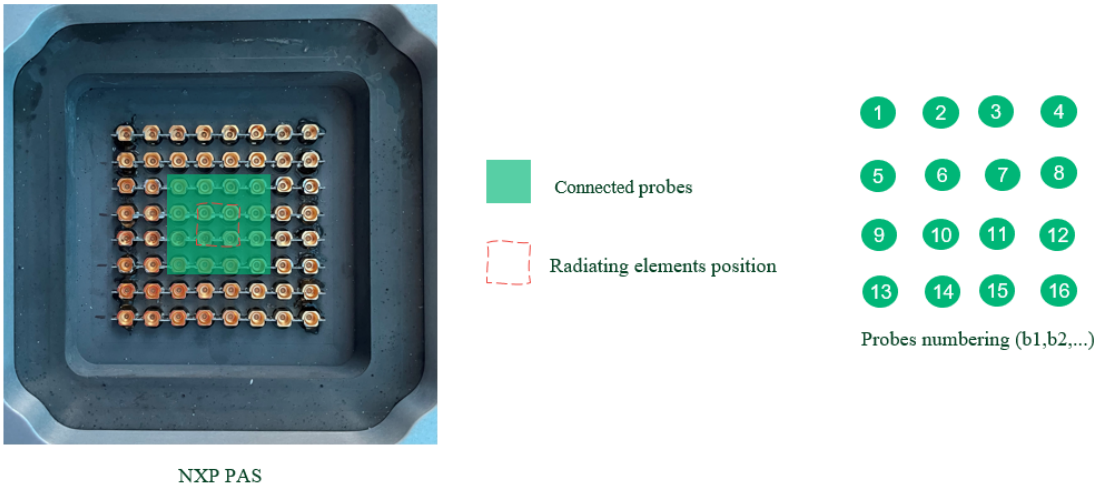

Figure 3.1: Scarif-DUT NXP-PAS Experiment schema

of evaluating the reconstruction performance when using the NXP PAS and exploiting different sets of probes (e.g. 16 probes, different sets of 4 probes ecc...)

in the reconstruction. In order to evaluate the reconstruction performance, either reference FF measurements (i.e., beam measurements in anechoic chambers) or reconstructions with the Scarif PAS are used. The metric is a simple visual consideration, one could in principle have a numerical evaluation (e.g. boreside error, ...) but this depends pretty much on the application of the technology. For the reconstructions, the same FF data was used: the differences are then due to different situations happening in the NF. As a final remark, probe i in the graphs is marked as b_i and this is just an arbitrary notation name.

3.1.1 Results NXP PAS and Scarif DUT

As we can see from Fig. 3.2, the selection of the probes has an impact on the reconstruction performance.

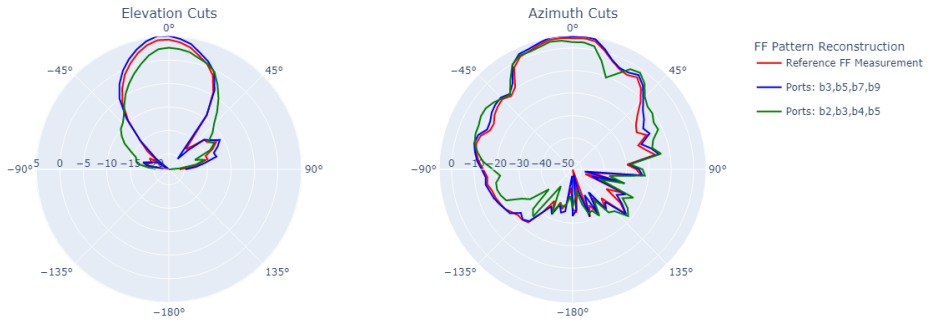

(a) Reconstructions with different probe sets VS FF beam measurement (red)

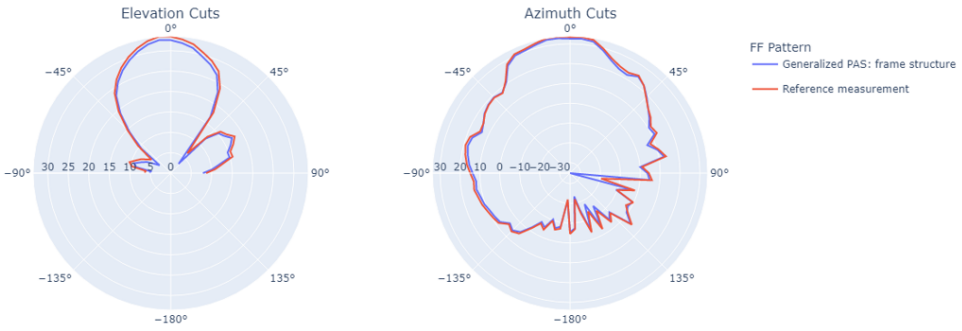

(b) Reconstruction with probes 1, 4, 13, 16 (blue) VS NF Reconstruction with Scarif PAS (red)

Figure 3.2: Generalized PAS reconstructions

An interesting feature appears when using all the available probes (Fig. 3.3). As we can observe, the effect of adding listening probes leads to worse or better results according to the selected subsets. This effect might be due to some interaction between the elements in the NF leading to some kind of interference that the least square optimization is not able to average out. In order to find out which might be the reason behind this effect, a singular value decomposition of the NF calibration data was analyzed. The reasoning behind it is that if in the entire experiment we change the amplitude and phase settings for only 4 of the antennas, we expect the calibration matrix P to have only 5 major singular values: the 4 antennas and the effect of the other elements, whose settings are kept constant, which account for an additional degree of freedom. Due to the noise, the other singular values are expected to be not exactly zero but much smaller than the main ones. If the system is not working properly then there might be a variation of the number of the major singular values, for instance if one of the emitting antenna is broken then we would have less major singular values. The calibration data is the P-matrix, i.e. the probes readings corresponding to 384 (4 antennas x 3 amplitudes x 32 phases) different single element settings. In Fig. 3.4 the SVD decomposition is shown, and we see that there are 5 major singular values.

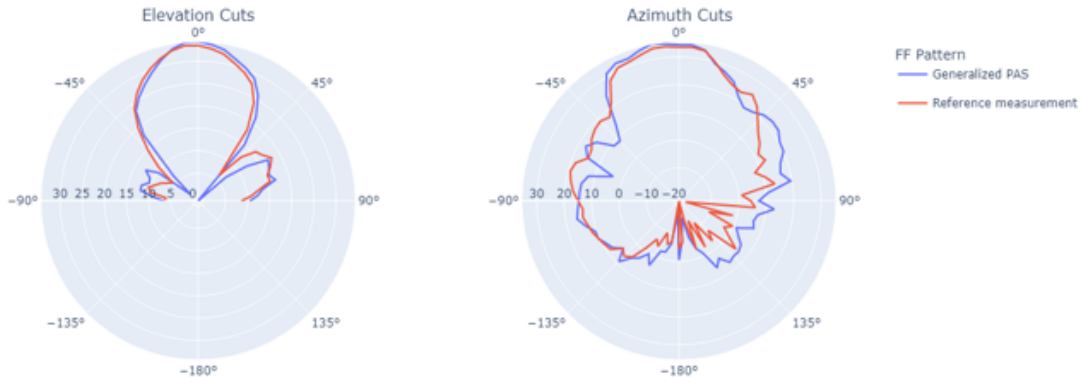

Figure 3.3: 16 probes reconstruction

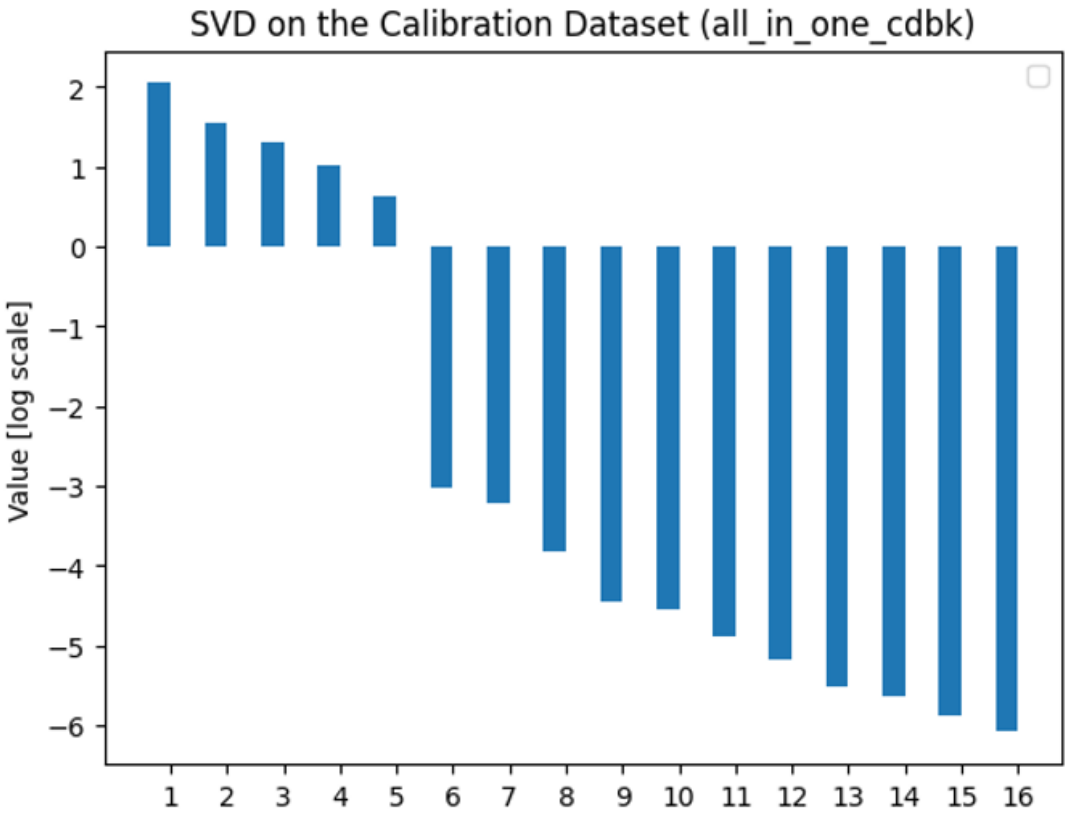

Figure 3.4: SVD on the P-matrix

SVD STUDY

An attempt to cope with this disturbance might be to exploit the SVD decomposition even further. Since we saw that selecting 4 probes, i.e. the minimum number of probes required, might lead to better performances with respect to use all of them, the idea was to select the best possible set of 4 probes that would lead to the best reconstruction performance. The first simple approach would be to compare the reconstruction of each group of 4 probes with a reference one, and select the best according to a given scoring function depending on the use cases. This method has multiple drawbacks:

1. It requires a FF reference beam measurement to compare with the reconstruction of each set of probes. This has to be repeated for each beam as the best set of probes might change.

2. The complexity scales exponentially with the number of probes as the possible combinations increase. Still, this is an offline procedure in the sense that for each beam the best probes can be found only once, as an additional calibration step, and then as long as the setup of the system is the same (i.e. same DUT type and same measurement conditions) the best probes for each beam don't change.

To overcome these issues, the idea is then to base the best 4-tuple probes selection on the major singular values with some kind of scoring criteria (e.g., get the probes that lead to the highest minimum singular value, the highest singular values, ecc...). The hope is then to apply this criteria when performing the calibration for a generic DUT, and so select the best probes for it. For this experiment, the reference measurement is a FF measurement carried out in the chamber with the classical methods. We can also define a singular-values reference, e.g. probes 1, 4, 13 and 16 that resulted in a good reconstruction (see Fig. 3.2b). In this experiment we used a subset of the listening probes from which to extract the 4-tuple probes to evaluate the heuristic criteria with (we used probes 1 to 9). This is because these probes were sufficient to evaluate the performance of the heuristic probe selection criteria, so extending the number probes taken into account would have led to an exponentially greater number of combinations to be scored and so an unneccessary long execution time of the Python script. We can see from Fig. 3.5 that unfortunately none of the scoring criteria lead to good results.

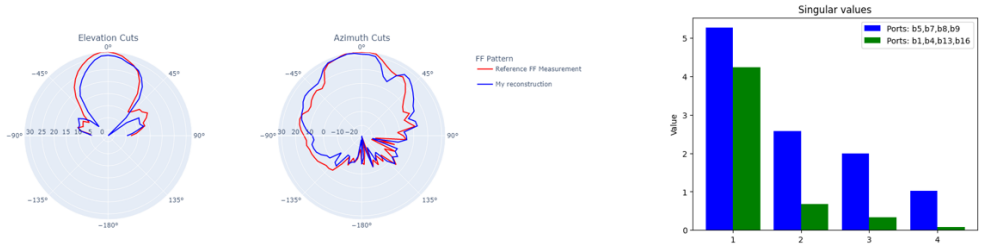

(a) Maximum last singular value

(b) Minimum last singular value

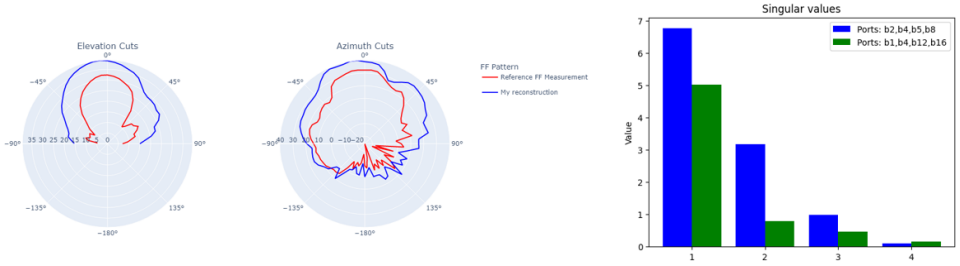

(c) Maximum first singular value

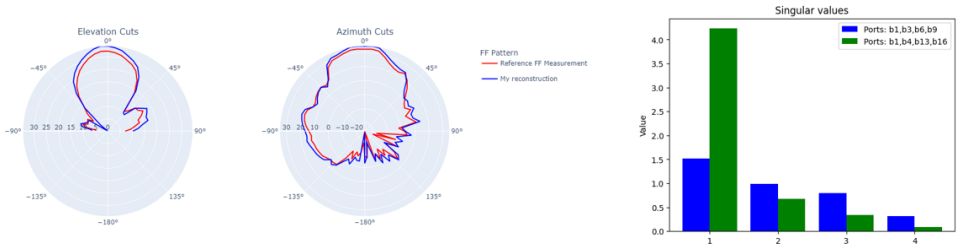

(d) Minimum first singular value

Figure 3.5: SVD scoring criteria performances

In order to evaluate if the problem was due to the PAS system, we also tried to use the Scarif PAS (i.e., the PAS specifically designed for the Scarif antenna) but with 16 listening probes. As we can see from Fig. 3.6, the problem is still present. This suggests that the issue might be caused by the antenna itself, the next experiment with the NXP DUT will clarify this aspect.

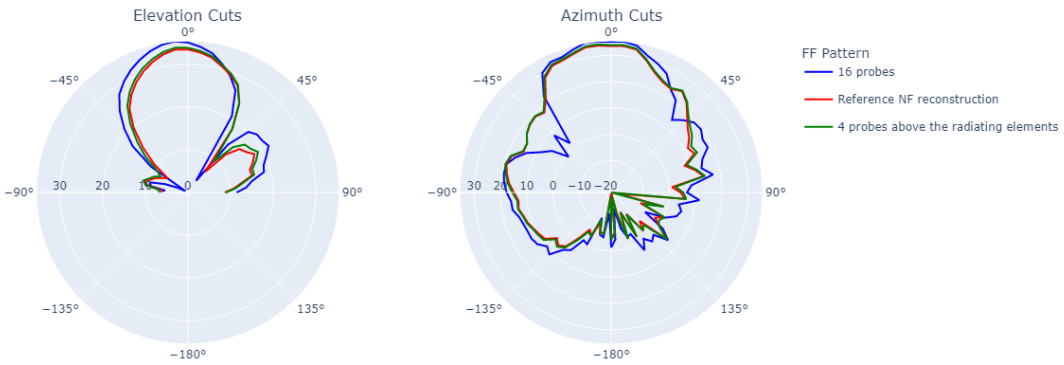

Figure 3.6: Scarif PAS and Scarif DUT reconstruction

3.2 Generalized PAS: NXP DUT

This experiment can be outlined as follow:

1. The NXP DUT is measured with its PAS but with different probes sets, in order to verify whether there is a similar behavior that the Scarif showed in Fig. 3.6 or not.
2. The NXP DUT is measured with its PAS but with different probe sets and alignments with respect to the emitting antennas.
3. The NXP DUT is measured with the Scarif PAS.

3.2.1 NXP PAS with different probe sets

The experiment conditions are listed as follow:

- SG output power: -3 dBm
- SA reference level: -13 dBm
- Frequency: 25.875 GHz
- Number of emitting antennas: 4
- Active elements configuration: 3 amplitudes and 32 phases
- Non-mutable (interfering) elements configuration: they are turned off
- PAS: NXP PAS

- Reference: NF reconstruction with the probes above the emitting elements, i.e. probes 6-7-10-11

The scenario is the same as before (fig. 3.1) but now the elements are aligned with the probes as we are using the NXP DUT.

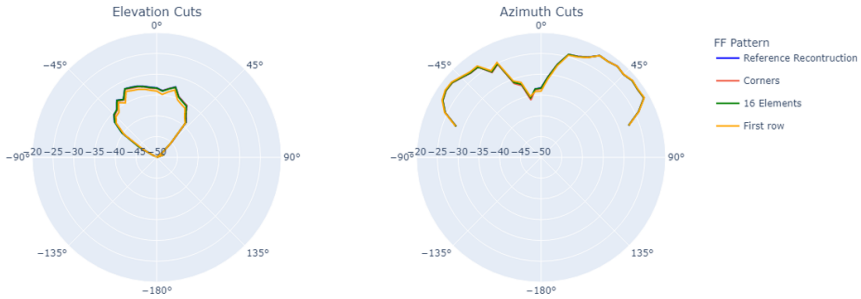

Figure 3.7: NXP DUT and NXP PAS reconstructions: corners = probes 1-4-13-16, first row = probes 1-2-3-4, 16 Elements = probes 1 to 16

Using different sets of probes seem not to impact the reconstructions, as it is expected (even though an higher number of probes should improve the SNR).

3.2.2 NXP PAS with different probes alignment

The experiment conditions are listed as follow:

- SG output power: -3 dBm
- SA reference level: -13 dBm
- Frequency: 25.875 GHz
- Number of emitting antennas: 4
- Active elements configuration: boreside with maximum amplitude
- Non-mutable (interfering) elements configuration: they are turned off
- PAS: NXP PAS

I tried a different alignment of the probes (Fig. 3.8) to check if it mattered. This is a crucial issue to verify the feasibility of future use cases where there will be a PAS "surface", and so no alignment between DUT antennas and probes.

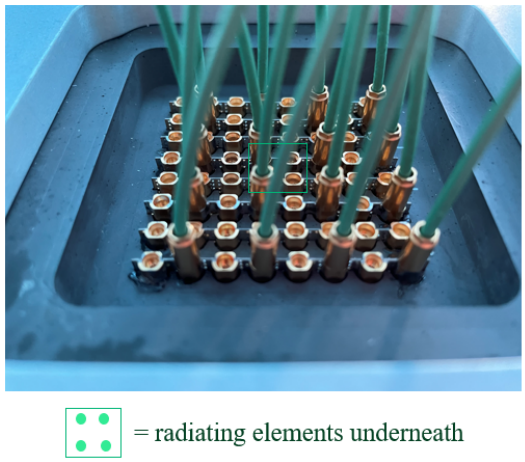

Figure 3.8: NXP DUT and NXP PAS: new probe alignment

We can see that the results (Fig. 3.9) are basically the same with the new and old alignments, moreover we can notice from Fig. 3.9b that using the farthest probes from the emitting elements causes a drop in the singular values , likely caused by lower SNR due to the distance, and consequently to slightly worse performance.

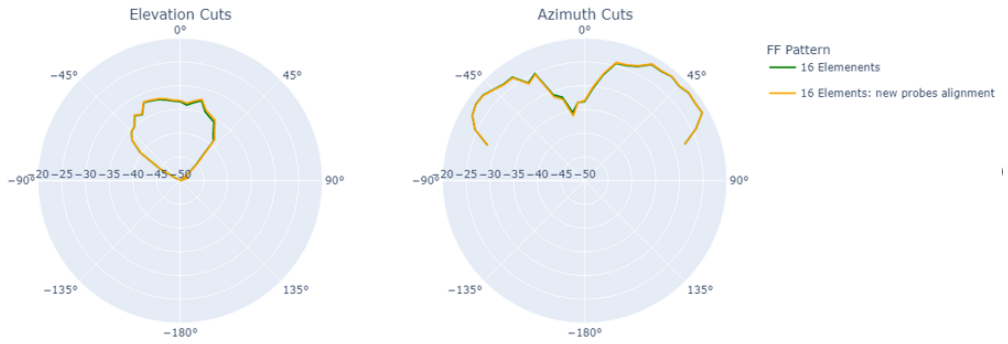

(a) 16 probes Old VS New alignment

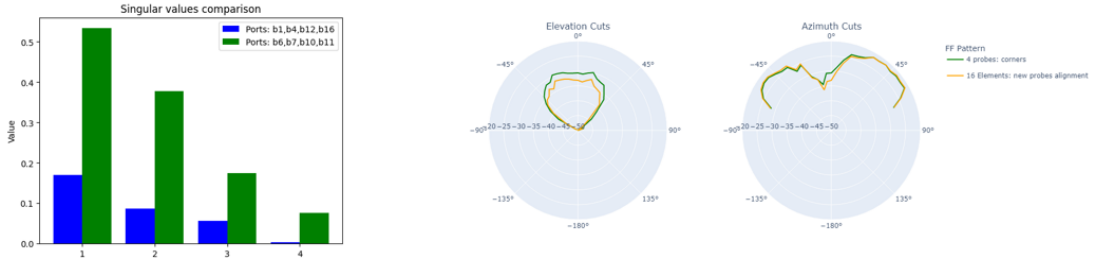

(b) 16 probes VS probes 1-4-13-16

Figure 3.9: New probes alignment performances

3.2.3 Scarif PAS

The experiment conditions are listed as follow:

- SG output power: -3 dBm
- SA reference level: -13 dBm
- Frequency: 25.875 GHz
- Number of emitting antennas: 4/16
- Active elements configuration: boreside with maximum amplitude
- Non-mutable (interfering) elements configuration: they are turned off
- PAS: Scarif PAS
- Reference: FF measurement in the chamber

Changing the set of the probes (within the same PAS) can be seen as using different PASs, as what differentiate one PAS from the others is the alignment of the probes. Still, it is useful to measure the NXP with the Scarif PAS and verify this claim. In Fig. 3.10 we can notice that the reconstructions with the different PAS systems are pretty much the same.

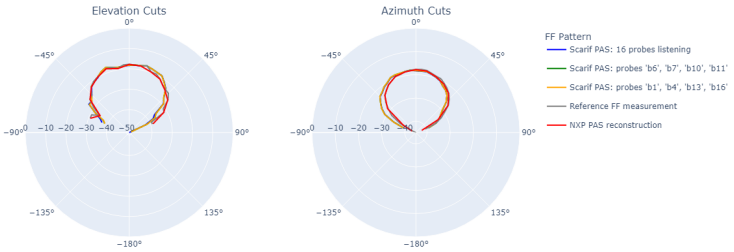

(a) 4 emitting antennas

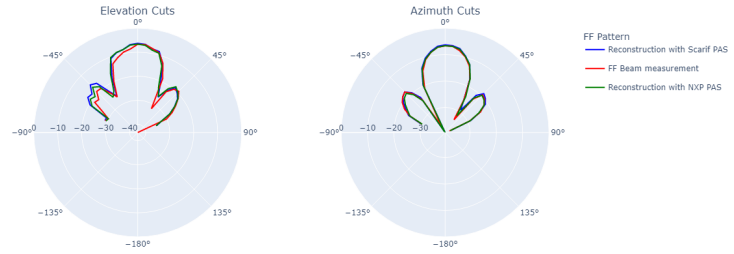

(b) 16 emitting antennas

Figure 3.10: Scarif PAS and NXP DUT

3.3 Conclusions and Future work

The experiment looks at how the reconstruction performance varies with respect to the selection of probes and the number of probes used to make the measurements. Expectations based on theory and EM simulations were that we should be able to reconstruct well for any number of probes greater or equal to the number of DUT elements, and for relatively arbitrary selection of probes. In particular, the method should work without requiring a one-to-one correspondence of element locations on DUT and PAS side and it should work even if the PAS was not specifically designed for the DUT. Comparing to expectation, the actual measurement results show that:

1. PAS design doesn't have to be very specific to the DUT. Still, this is just a promising indication given the limited statistics.
2. Using more than the minimum number of probe elements is possible.
3. Moving probes farther away from the active DUT elements seems to make readings less reliable and reduces reconstruction performance.
4. Measurements on DUTs with active immutable elements seem to be sensitive to the specific probe selection; while the reason has not been fully identified yet, a next step can be to further optimize the handling of the immutable elements either through using an additional probe to capture the corresponding additional degree of freedom, or through changes in the configuration of calibration measurements (i.e, changing the reference setting $\boldsymbol{w}_0$). It must be pointed out that the Scarif antenna is not a commercial antenna but rather a proof of concept while the NXP is still a prototype but much more tested and reliable compared to the Scarif. In order to extend this study one can try others heuristic strategies or using more probes than 4. For instance using 5 probes would capture also the effect of the non-mutable elements and these might lead to different results, especially in the case where the minimum singular value is concerned.

4

Improving the speed of DUT Rx Measurements

A challenge with the previously implemented method for DUT Rx measurements described in Section 2.5 is that we need to carry out a separate NF measurement for each direction along which we want to evaluate the DUT response. This issue is stressed in all the use-cases where patterns need to be evaluated with a fine spatial resolution or over a larger set of directions. pattern evaluations are required. With this new method, after a first calibration, it is sufficient to carry out a number of NF measurements equal to the number of DUTs antennas, independently of the number of pattern points.

4.1 Pattern RX reconstruction algorithm

Instead of emulating the radiation of an EM wave coming from the FF as done in the Sparse point RX reconstruction algorithm, we generate a radiation from the PAS such that it excites one antenna only (ideally). Exciting one DUT element only means we can interpret the DUT output as the response of that DUT element to the field and as a weighting factor for its single-element RX pattern. By cycling through all DUT elements in this manner, the full-beam DUT RX pattern is found as their superposition. We still aim to reconstruct the RX sensitivity pattern of the DUT in response to plane waves coming from

different directions in the FF as shown in Fig. 4.1, i.e., we aim to reconstruct:

$$\begin{aligned} a_{FF}(\boldsymbol{w}, \theta_m, \phi_m) &= \sum_{n=1}^{N} c_n(w_n) s_n(\theta_m, \phi_m) \\ &= \boldsymbol{c}(\boldsymbol{w})^T \boldsymbol{s}(\theta_m, \phi_m) \end{aligned} \tag{4.1}$$

where $s_n(\theta_m, \phi_m)$ is the single element RX pattern (scaled by the source input signal in the FF b_m).

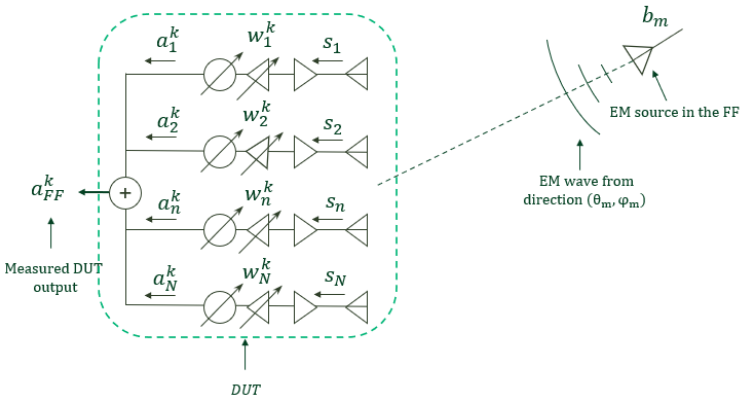

Figure 4.1: DUT Rx response to a plane wave excitation from a FF source at one direction

The main idea is to estimate some kind of weighting factors and exploit them to overlap the single element RX patterns. The definitions of weighting factors and single element patterns are the following:

1. *Weighting factor*: the weighting factors that we will use to overlap the single element patterns are

$$c'(w_n) = s_{ref,n} c_n(w_n) \tag{4.2}$$

where $s_{ref,n}$ is a reference excitation with which we are stimulating the antenna n. In other words, the weighting factor $c'(w_n)$ is nothing but the output of the DUT if we are exciting the DUT element n only and if the element setting is w_n.

2. *Single element pattern*: Like in the first RX method, it is the quantity $s_n(\theta_m, \phi_m)$.

Now if we superimpose the elements we end up with:

$$\begin{aligned} a'_{FF}(\boldsymbol{w}, \theta_m, \phi_m) &= \sum_{n=1}^{N} c'_n(w_n) s_n(\theta_m, \phi_m) \\ &= \sum_{n=1}^{N} s_{ref,n} c_n(w_n) s_n(\theta_m, \phi_m) \end{aligned} \tag{4.3}$$

If we now are able to excite each antenna in the same way (i.e., $s_{ref,n}$ is constant across the DUT antennas) then we have:

$$\begin{aligned} a'_{FF}(\boldsymbol{w}, \theta_m, \phi_m) &= s_{ref} \sum_{n=1}^{N} c_n(w_n) s_n(\theta_m, \phi_m) \\ &= s_{ref} \cdot a_{FF}(\boldsymbol{w}, \theta_m, \phi_m) \end{aligned} \tag{4.4}$$

i.e., a version of the actual RX pattern scaled by the strength of the excitation. In order to stimulate in the NF each antenna in the same way, we can exploit the F_{NF} matrix found in the calibration phase. In fact the reconstruction matrix F_{NF} is the same as in the first RX method. We can just exploit $\boldsymbol{F}_{NF}$ to produce a set of stimuli $\boldsymbol{p}$ from the PAS such that at the DUT antenna outputs we have:

$$\boldsymbol{s}_{NF}(\boldsymbol{p}) = \boldsymbol{F}_{NF} \cdot \boldsymbol{p} = [0, ..., s_{ref}, ..., 0]^T \tag{4.5}$$

i.e., we are stimulating only one DUT antenna at a time. From (4.5) we can see that the corresponding stimuli achieving that is:

$$\boldsymbol{p}_n = \boldsymbol{F}_{NF}^{-1}[0, ..., 1, ..., 0]^T s_{ref} \tag{4.6}$$

i.e., the the n_{th} column of $\boldsymbol{F}_{NF}^{-1}$ scaled by the desired excitation s_{ref}. We can then record the DUT response to that stimulus, i.e. $c'(w_n)$, and then repeat the procedure for all the DUT antennas. Doing so we are able to find the weighting factors that each branch has in the RX pattern, given a generic configuration. The whole procedure can be schematized as follow:

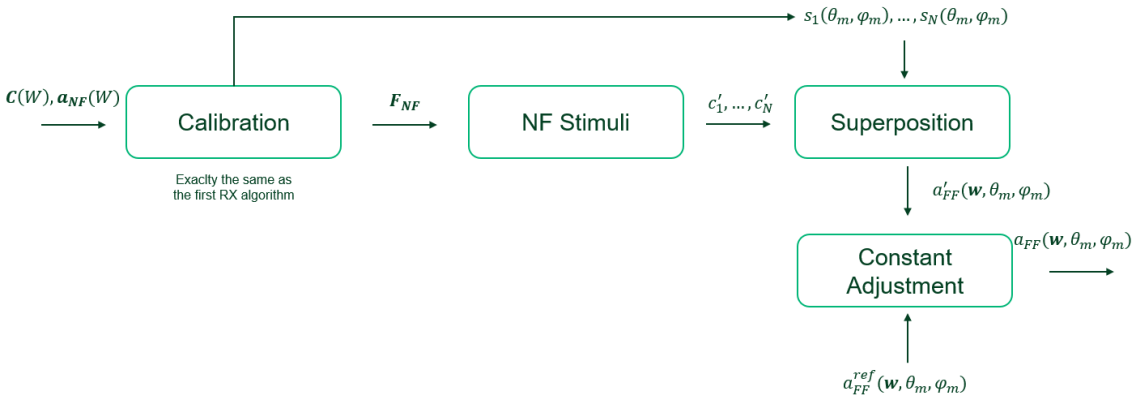

Figure 4.2: Pattern RX reconstruction algorithm

Note that in the "Constant Adjustment" phase a reference FF beam measurement is used in order estimate the scaling factor s_{ref}. At the current implementation, this constant is estimated averaging the ratio between the reference FF measurement and the reconstructed pattern. Not the whole pattern is used, but only the portion $\leq 3dB$ with respect to the maxima. This estimation needs to be carried out only once, and can be seen as another calibration step of the system.

4.2 Practical Implementation

Moreover here, we need to use the estimations of the quantities we need. These quantities have been defined and estimated through FF measurements in Section 2.3:

- Coupling matrix estimation: $\tilde{\boldsymbol{F}}_{NF} = \boldsymbol{C}(\boldsymbol{w}_0) \cdot \boldsymbol{F}_{NF}$
- Weighting factor estimation: $\tilde{c}_n(w_n) = \dfrac{c_n(w_n)}{c_n(w_0)}$
- Single element pattern estimation: $\tilde{s}_n(\theta_m, \phi_m) = c_n(w_0) s_n(\theta_m, \phi_m)$

We can show now that using these estimations in place of the true values will end up with the same sensitivity pattern reconstruction expression (4.4). If we use $\tilde{\boldsymbol{F}}_{NF}$ in place of $\boldsymbol{F}_{NF}$ in (4.6) we will end up with an estimation of the true stimuli $\boldsymbol{p}_n$:

$$\begin{aligned} \tilde{\boldsymbol{p}}_n &= \tilde{\boldsymbol{F}}_{NF}^{-1}[0, ..., 1, ..., 0]^T s_{ref} \\ &= \boldsymbol{F}_{NF}^{-1} \boldsymbol{C}(\boldsymbol{w}_0)^{-1}[0, ..., 1, ..., 0]^T s_{ref} \\ &= \boldsymbol{F}_{NF}^{-1}[0, ..., s_{ref}/c_n(w_0), ..., 0]^T \end{aligned} \tag{4.7}$$

we can compare now (4.6) and (4.7) and see that the DUT antennas output that $\tilde{\boldsymbol{p}}_n$ will produce is:

$$\boldsymbol{s}_{ref,n} = [0, ..., s_{ref}/c_n(w_0), ..., 0]^T \tag{4.8}$$

This means that using the estimations we are stimulating only the DUT target antenna, but the resulted excitation is not equal across the antennas. In other words, when we are targeting antenna n, the output of that antenna is equal to $s_{ref}/c_n(w_0)$ while the other elements are not excited. Since now we have the estimations of the single element patterns $\tilde{s}_n(\theta_m, \phi_m)$, we can now rewrite (4.4) with the antennas outputs $\boldsymbol{s}_{ref,n}$ (4.8) and single element estimations $\tilde{s}_n(\theta_m, \phi_m)$:

$$\begin{aligned} \tilde{a}'_{FF}(\boldsymbol{w}, \theta_m, \phi_m) &= \sum_{n=1}^{N} s_{ref,n} c_n(w_n) \tilde{s}_n(\theta_m, \phi_m) \\ &= \sum_{n=1}^{N} \frac{s_{ref}}{c_n(w_0)} c_n(w_n) c_n(w_0) s_n(\theta_m, \phi_m) \\ &= s_{ref} \cdot a_{FF}(\boldsymbol{w}, \theta_m, \phi_m) \end{aligned} \tag{4.9}$$

which is exactly (4.4).

In Fig.4.3 we have a comparison between the reconstruction performances of the two RX algorithms and a FF measurement carried in the chamber. The measured antenna is the Scarif with 4 active antennas at 28 GHz.

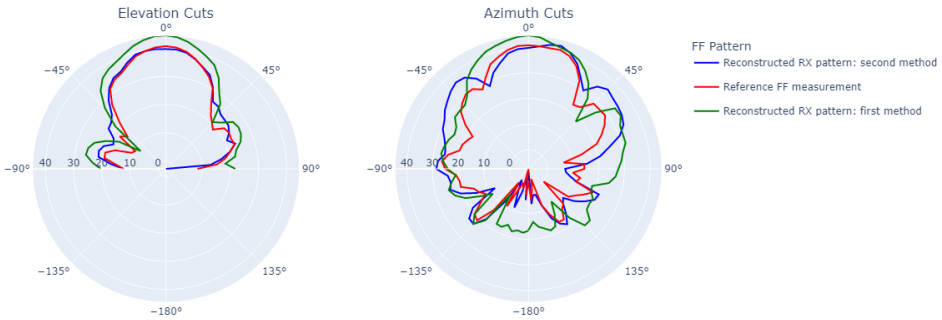

(a) Beam 1

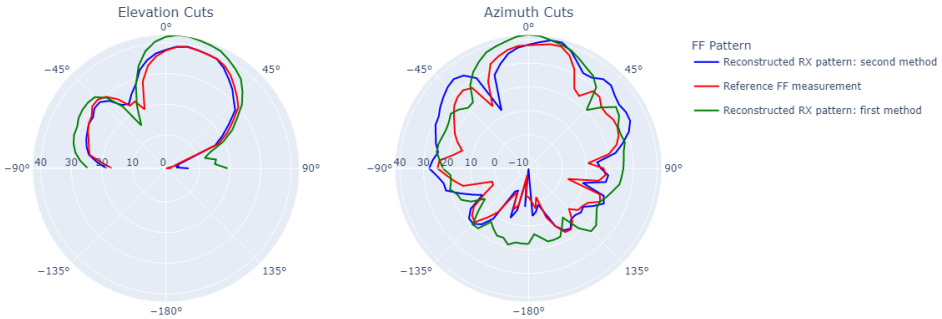

(b) Beam 2

Figure 4.3: RX algorithms performance: in green the Sparse point RX reconstruction (first method), in blue the Pattern RX reconstruction (second method)

In figure (4.4) we can see the reconstruction performances of the Pattern RX reconstruction algorithm compared with the optimal reconstruction weights for beam 1. The optimal weights $\boldsymbol{c}^*$ for the beam 1 are the result of the minimization of

$$\boldsymbol{c}^* = argmin_{\boldsymbol{c}} \| \sum_{n=1}^{N} c_n s_n(\theta_m, \phi_m) - a_{FF}(\boldsymbol{w}_1, \theta_m, \phi_m) \| \tag{4.10}$$

i.e., an upper bound to the reconstruction performances given the quality of the single element measurement $s_n(\theta_m, \phi_m)$.

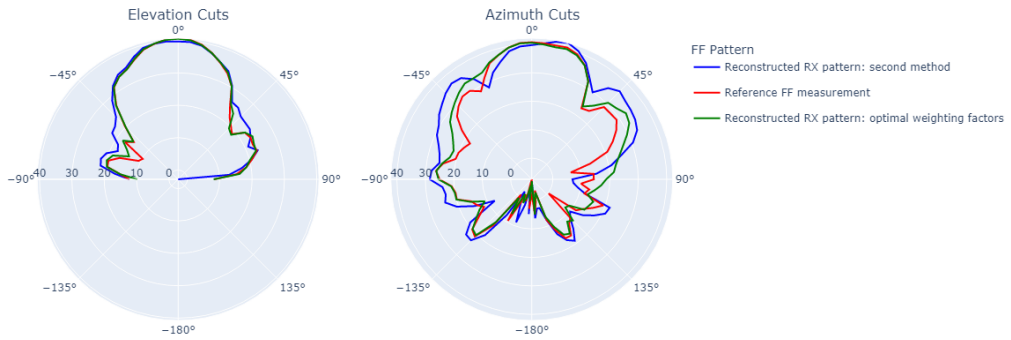

Figure 4.4: Reconstruction with optimal weights VS Pattern RX reconstruction algorithm

In order to evaluate how well we are stimulating each antenna, and the correctness of the model and scripts, the DUT in which only one antenna was active was tested. In this case, we expect the weighting factor corresponding to that antenna to be much higher compared to the others. For this experiment, the Scarif at 28 GHz with four emitting antennas was used. In tab.5.2 the estimated weighting factors.

Active Antenna	$\lvert c_1 \rvert$	$\lvert c_2 \rvert$	$\lvert c_3 \rvert$	$\lvert c_4 \rvert$
1	-14.05	-23.08	-22.02	-26.77
2	-28.76	-15.03	-34.13	-24.92
3	-34.00	-29.99	-13.83	-29.96
4	-39.06	-27.58	-30.93	-13.11

(a) Amplitudes [dBV]

Active Antenna	$\angle c_1$	$\angle c_2$	$\angle c_3$	$\angle c_4$
1	133	93	126	129
2	33	133	-19	-164
3	138	119	142	109
4	38	142	-2.55	153

(b) Phases [deg]

Table 4.1: Estimated weighting factors

4.3 FF Interference compensation

The interference so far is used in the calibration phase to find the matrix F_{NF}, but not in the single element FF data. To tackle this we used an interference pattern, i.e. the pattern produced by the elements when they are in off state and subtracted from each single element data before the superposition. Since the FF beam measurement used to evaluate the reconstruction contains the interference pattern (the effect of the immutable elements is present in the FF measurement as well), the interference pattern must be added to the superposition. Before adding it as a last step, the interference pattern was scaled by the complex constant found with the FF reference pattern as the weighted sum of the single element is a scaled version of the true pattern. In figure (4.5) we can see that this further interference compensation slightly improves the results.

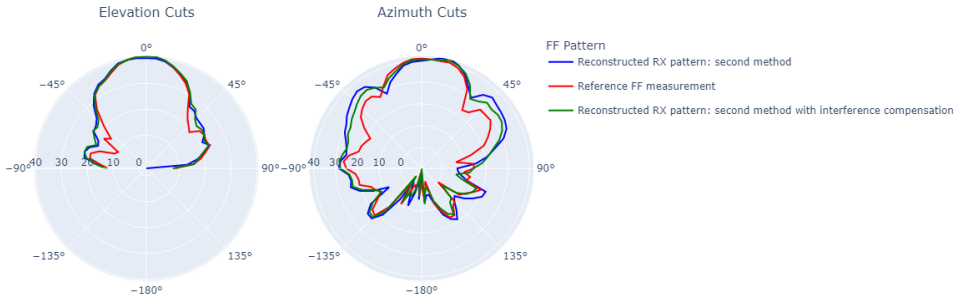

(a) Beam 1

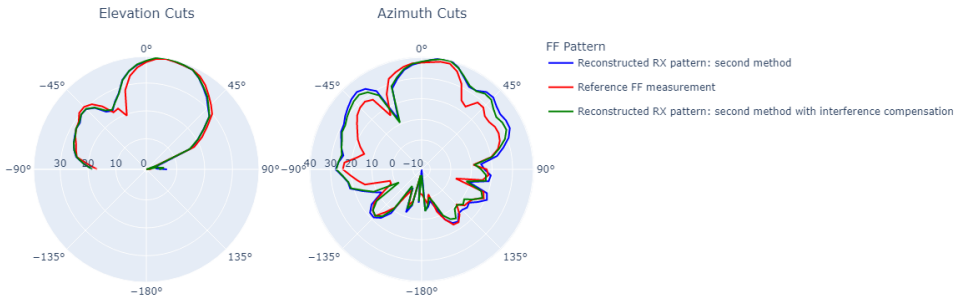

(b) Beam 2

Figure 4.5: Performances at 28 GHz with interference compensation

4.4 Conclusions and further improvements

We can see from table 5.2 that we are able to obtain a good isolation between the target element and the others. Still it must be pointed out that here we are not seeing the excitation produced by the active PAS directly, as we are watching the output of the DUT caused by that stimulus. If one want to ascertain more in detail on how well we are able to excite each antenna, then the solution would be using another VST as a DUT that can sense each port separately. Another critical point is that in the current implementation we are forcing isolation (excite only the target, and not the others) between the 4 active elements. Still we don't have control on the situation in the NF where the other 12 elements are off. To carry out this evaluation, we would need also here a multi-port VST and sense how the global situation in the NF is. Overall this new RX method is comparable, or slightly better, than the old one but it is much faster in the use cases where the number of antennas is much less than the number of points of the pattern we are interested to evaluate.

5

Beam Formed PAS

One of the main problems for the PAS technology is the cost of the required system. What drives its cost is mainly the number of instrument channels, that scales with the number of probe elements which, in turn, scale with the number of DUT element. This is particularly true for the RX case testing as all probes need to generate at once to create a specific EM field across the DUT aperture. The goal would be having a single instrument channel, independent of the DUT number of elements. In order to achieve that, the idea is to exploit a beam former at PAS side, and replace a parallel drive/read of the probes with subsequent feeds/measurements. This chapter analyzes how to exploit a beamformer in both TX and RX characterizations.

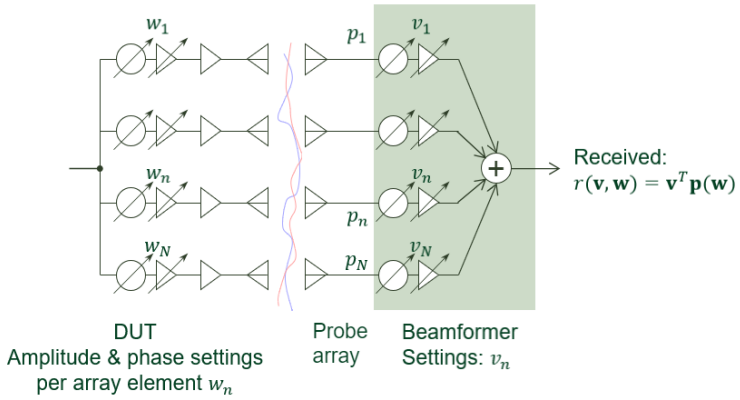

Figure 5.1: BF PAS Scheme

5.1 BF PAS IN DUT TX

Instead of performing N parallel measurements to obtain the NF indications $\boldsymbol{p}(w)$, we can perform N subsequent measurements to obtain the vector

$$\boldsymbol{r}(w) = [r_1 = \boldsymbol{v_1}^T \boldsymbol{p}(w), ..., r_N = \boldsymbol{v}_N^T \boldsymbol{p}(w)]^T = \boldsymbol{V} \cdot \boldsymbol{p}(w) \tag{5.1}$$

In equation (5.1) the NxN matrix $\boldsymbol{V}$ is defined s.t. its i-th row is the $\boldsymbol{v}_i^T$ vector. If the $\boldsymbol{v}_i$ are linearly independent, we can obtain a 1-to-1 correspondence between the NF indicators $\boldsymbol{p}(w)$ and the subsequent measurements $\boldsymbol{r}(w)$, as V would be full rank. This fact can be exploited to reuse the equations found in Chapter 2 and Appendix A. In fact, we have the relations:

$$\boldsymbol{c}(w) = \boldsymbol{G}\boldsymbol{p}(w) \tag{5.2}$$

where $\boldsymbol{G}$ is the calibration matrix. We can then exploit the invertibility of V to write

$$\boldsymbol{p}(w) = \boldsymbol{V}^{-1}\boldsymbol{r}(w) \tag{5.3}$$

We can then rewrite (5.2) as

$$\boldsymbol{c}(w) = \boldsymbol{G}\boldsymbol{p}(w) = \boldsymbol{G}\boldsymbol{V}^{-1}\boldsymbol{r}(w) = \boldsymbol{U}\boldsymbol{r}(w) \tag{5.4}$$

We now have a new model, in which we relate the weighting factors $\boldsymbol{c}(w)$ to the subsequent measurements $\boldsymbol{r}(w)$ by means of the matrix $\boldsymbol{U} = \boldsymbol{G}\boldsymbol{V}^{-1}$. We can perform the interference compensation by subtracting from the measured $\boldsymbol{r}(w)$ the interference $\boldsymbol{r}(w_{inter}) = \boldsymbol{V}\boldsymbol{p}(w_{inter})$ as it was done for G in the preceding analysis (see Appendix A). We can now proceed to estimate the matrix $\boldsymbol{U}$ as it was done in the preceding analysis. In particular we can solve a Least Square minimization procedure using a sufficiently large set of settings w.This corresponds to:

$$\boldsymbol{U} = argmin_{\boldsymbol{A}} ||\boldsymbol{C} - \boldsymbol{A}\boldsymbol{R}||^2 \tag{5.5}$$

where the matrix R is defined as:

$$\boldsymbol{R} = [\boldsymbol{r}(w_1), ..., \boldsymbol{r}(w_p)] = [\boldsymbol{V}\boldsymbol{p}(w_1), ..., \boldsymbol{V}\boldsymbol{p}(w_p)] = \boldsymbol{V}\boldsymbol{P} \tag{5.6}$$

One could in principle drive the BF PAS in order to obtain the same effect

that a "parallel" read of the probes would produce, by using one single output line. From (5.3) we have

$$\boldsymbol{p} = \boldsymbol{V}^{-1}\boldsymbol{r} \tag{5.7}$$

i.e., we can reconstruct the reading outputs $\boldsymbol{p}$ via successive measurements $\boldsymbol{r}$. Note that this is actually a generalization of the current system: in fact, the probes are "virtually" read in parallel as in practice there is a switching matrix that listens to one probe per time. This is equivalent to have a beam former with $\boldsymbol{V} = \boldsymbol{I}$ with $\boldsymbol{I}$ the identity matrix. Since we use a "switched" passive PAS we already have a particular working implementation of a BF PAS in the DUT Tx. However, the BF PAS is critical for the DUT Rx and this will be studied in the next section.

5.2 BF PAS IN DUT RX

In both DUT RX testing approaches we need to be able to create a certain configuration of the NF. This translates into generating in parallel some input signals $\boldsymbol{p}$ at the PAS side by the signal generators. We can replace the SGs with a beam former, and using only one SG to drive it and obtain the same result:

$$\boldsymbol{p} = \boldsymbol{v} \cdot a_{in} \tag{5.8}$$

where $\boldsymbol{v} = [v_1, ..., v_m]^T$ are the beam former settings and a_{in} the input signal from the VST to the PAS. Even though this is a trivial consideration from a theoretical viewpoint, it is not the case in practice as other problems arise. Since the objective is to use a commercial beam former, we have much lower degrees of freedom on the signals that it is able to produce compared to a much more expensive measurement instrument.

5.2.1 NXP DUT AS A BF PAS

In order to test the feasibility of the approach, an experiment was carried out to examine how accurately a desired field distribution across the DUT antennas can be produced in the NF of the probe array using a common source signal and a commercial beamformer IC to modify the outputs of the probe array elements. In this experiment, we replace the actual DUT by a passive PAS so that we can observe directly the generated EM field at the points sampled by the DUT

antennas. Furthermore, we consider the NXP active antenna as our prototype beamforming probe array. The experimental setup is illustrated in Fig. 5.2. Note that while this setup is the same as previously shown for measuring DUT TX characteristics in Fig. 2.13 of Section 2.3.2, here the DUT and probing roles of the antennas on the transmitting and receiving side have been swapped.

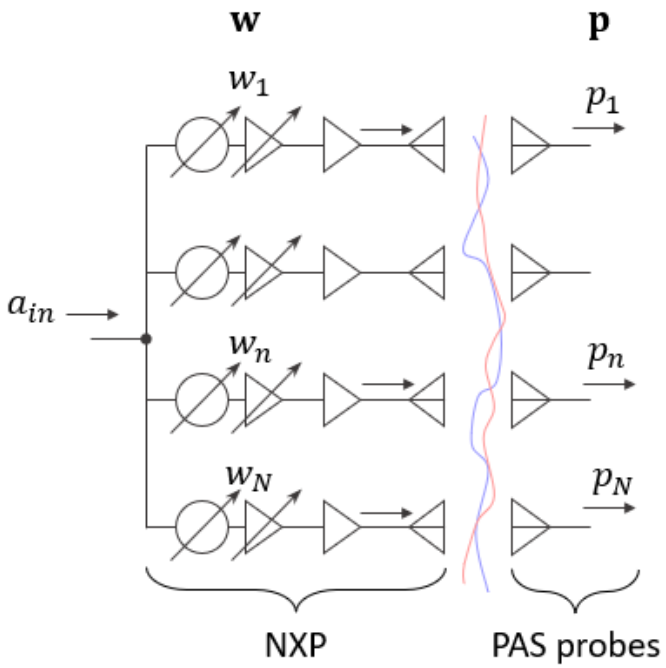

Figure 5.2: NXP as BF PAS experiment schema

Focusing on the second DUT Rx measurement method describe in Chapter 4, the BF PAS prototype should generate the desired EM field magnitude at only one of the Rx antennas. The response generated at all other Rx antennas should be very small (or vanish ideally). As a first approach, *linearity* between the array elements' amplitude and phase settings and realized outputs from the NXP antennas is assumed. Figure 5.3 shows the measured relation, in there both phases and gain settings are reported as 8-bit integer numbers to control the NXP active antenna. The gain setting index spans the whole dynamic range of the NXP single antennas, while the phase setting index step corresponds to $360°/255 \simeq 1.41°$. The figure presents at the behavior of NXP array element 36, one of the elements that are active in most of the measurements. Based on our data, the other elements show similar characteristics. The data was obtained in NF measurements with the passive PAS from the receiving element directly

above the NXP antenna element 36.

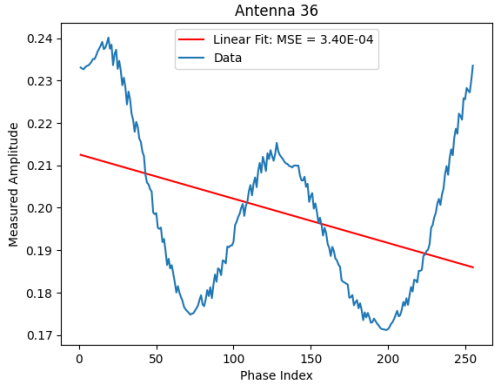

(a) Realized Amplitude VS Phase Setting

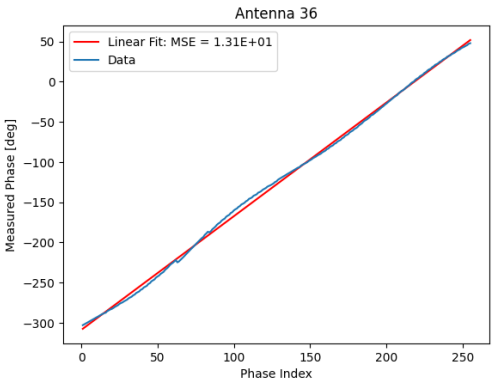

(b) Realized Phase VS Phase Setting

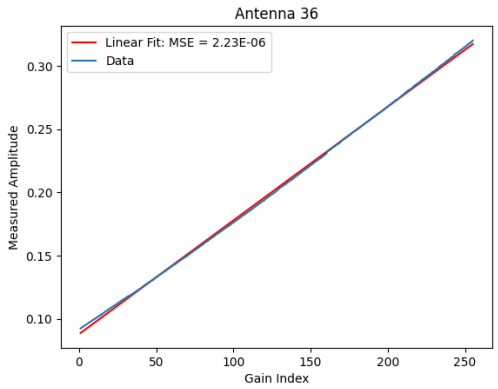

(c) Realized Amplitude VS Gain Setting

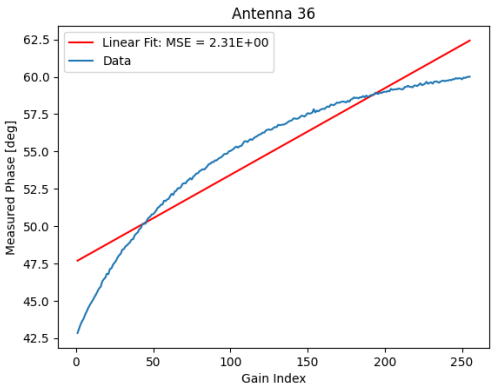

(d) Realized Phase VS Gain Setting

Figure 5.3: Relation between settings and antenna output: fixed gain index = 160, fixed phase index = 89

From Fig.5.3b and Fig. 5.3c the relation between setting and antenna output seems to be linear. In Fig.5.3a and Fig.5.3d we see that some non-linearity is present, because changing the gain has a (non-linear) effect on the realized phase and vice versa. We would have expected horizontal lines, as ideally changing the gain should not have any effect on the phase and vice-versa. This effect is due to how the BF circuits operate: changing gain means that more gain stages may be added, which may cause additional delay (i.e., phase variations) of the signal. Changing the phase means adding a delay which is implemented by making the signal travel different distances, and so we end up with different attenuations. Performing a linear Least Square approximation means to linearize these effects.

An important remark is that these effects were present also in the algorithms used for the TX and RX case and this might lead to the conclusion that the linear models used are wrong. This is not true. In fact both in the DUT TX

and RX case the linearity is exploited in the mapping between NF and FF, not from the DUT settings and the NF (or FF): in principle all the functions $c_n(w)$ can perfectly be non-linear. This effect can be appreciated in Fig. 5.4 where the ratio between NF and FF measurements (measured with the same DUT setting variations) is shown. The set of amplitudes/phases used to generate those data spans 3 amplitudes and 32 phases per element, in the figure the data refers to the antenna located under probe 1.

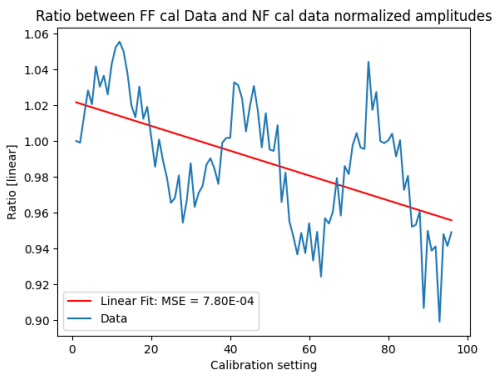

(a) Ratio between FF and NF measurements amplitudes (Normalized)

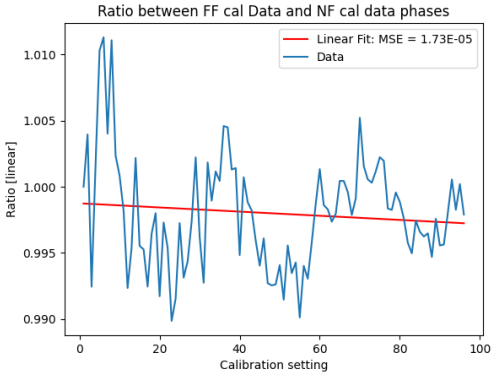

(b) Ratio between FF and NF measurements phases

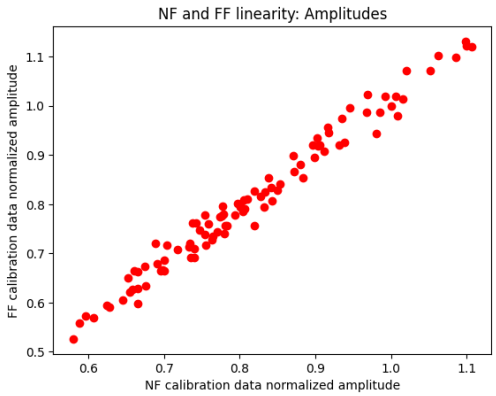

(c) NF VS FF calibration data amplitudes

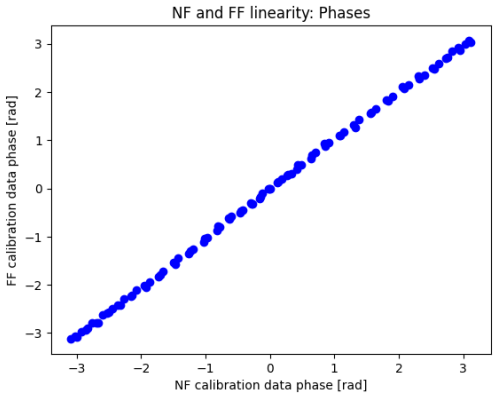

(d) NF VS FF calibration data phases

Figure 5.4: NF and FF linearity assumption verification

Since the relation between the antenna outputs and probes output in the NF is linear (through the calibration matrix F_{NF} in the DUT RX case), then we can map the NXP settings $\boldsymbol{w}$ to the PAS probes outputs $\boldsymbol{p}$ as:

$$\boldsymbol{p} = \boldsymbol{v} \cdot a_{in} = \boldsymbol{T} \cdot \boldsymbol{w} \tag{5.9}$$

We can then find the transformation matrix $\boldsymbol{T}$ via least square method, in a similar way as the DUT TX case (instead of mapping probe readings to realized weighting factors, here we are trying to map NXP settings to probe readings). We can then invert the matrix $\boldsymbol{T}$ and find the settings to feed the DUT with in order to obtain the desired PAS outputs, i.e.:

$$\boldsymbol{w} = \boldsymbol{T}^{-1} \cdot \boldsymbol{p} \tag{5.10}$$

Here we have two main problems: the first one is that, unlike the VST, the NXP has discrete amplitudes and phases settings as both have an 8 bit register available (i.e., 256 values). A rounding of the settings is then needed for feasibility. The second issue is the beamformer dynamic range.

A first test to evaluate the performances is trying to write the same excitation to each target probe, while the others should not be affected. This translates to a target reading of the type:

$$\boldsymbol{p} = [0, ..., 0, p_i, 0, ..., 0]^T \tag{5.11}$$

where p_i is a real number kept constant for all the target antennas. In this experiment 4 emitting antennas were used, and the 4 probes located on top of them were the targets. The resulting setting (i.e., amplitude and phase for each antenna) was scaled in such a way that the maximum amplitude would match the maximum single element one, in order to exploit (and not exceed) the dynamic range available. Due to this normalization we potentially lose the control on the reading amplitude but we gain in terms of isolation between the target probe and the others.

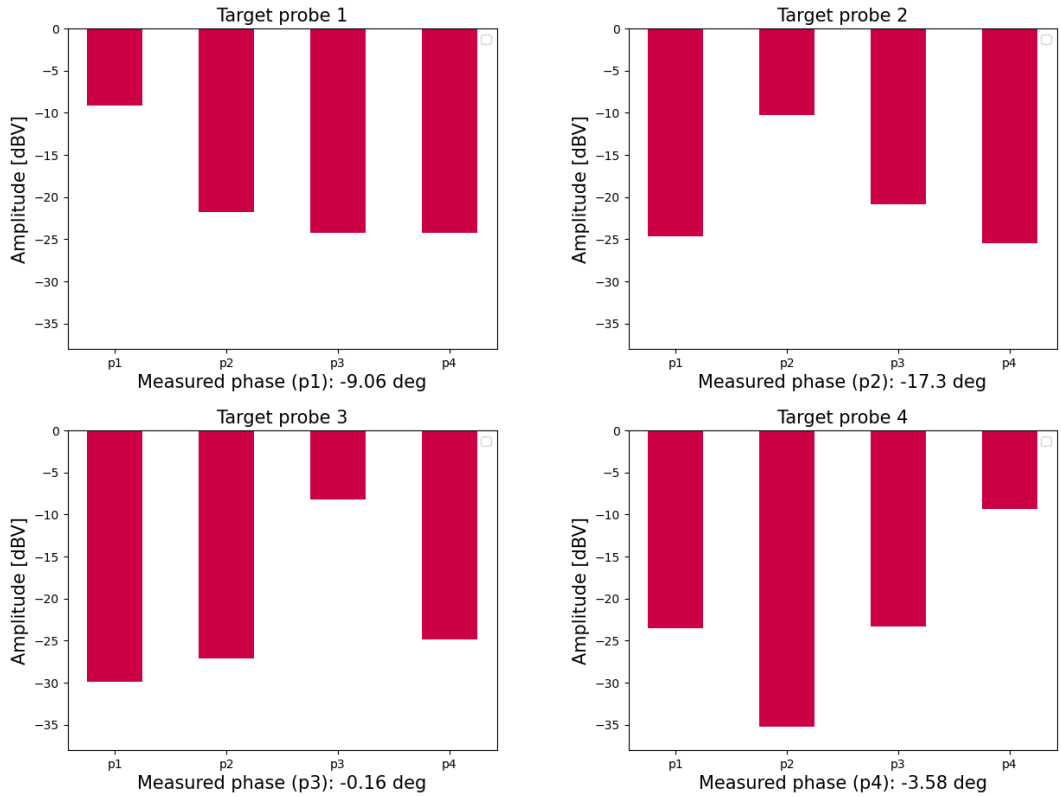

Figure 5.5: NXP DUT as a PAS: performances

In Fig. 5.5 we can see that we are able to excite in a "similar" way all the target probes (3 or 4 dBV of difference) with a phase error of 17.3 degrees in the worst case (with a real target, we would have expected phase of 0 degrees for all the target probes).

The second experiment consists of trying to reconstruct the settings that produced a known situation in the NF, and compare it with the true one. In other words, given a PAS reading $\boldsymbol{p}$ we exploit equation (5.10) to estimate the setting $\boldsymbol{w}^*$ that produced it. Then, we compare it with the true one, that is known.

Antenna	True Amplitude	True Phase	Reconstructed Amplitude	Reconstructed Phase
1	255	89	321	89
2	255	208	295	205
3	255	81	334	82
4	255	214	290	215

Table 5.1: Beam 0 setting reconstruction performances

Antenna	True Amplitude	True Phase	Reconstructed Amplitude	Reconstructed Phase
1	100	10	134	3
2	100	20	123	12
3	200	30	182	25
4	200	40	166	37

Table 5.2: Beam 1 setting reconstruction performances

A third experiment consists of abandoning the linearity assumption and using other techniques to create a certain configuration in the near field, i.e. apply a *Delaunay Triangularization* [12] on the NF data. In particular a single NXP antenna as well as a single PAS probe was used. The antenna spanned settings of amplitude and phases, and the probe responses were recorded. This data have been triangularized, and then used to obtain a target situation in the NF (i.e., a target probe reading). In Fig. 5.6 a visual scheme is presented aimed to better clarify what a data triangularization means.

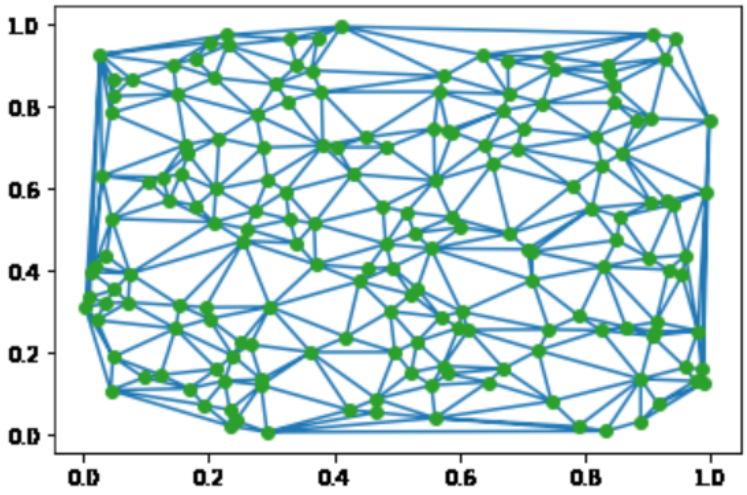

Figure 5.6: Delaunay Triangularization on the green data points. Picture taken from https://www.geeksforgeeks.org/triangulations-using-matplotlib/

In Fig. 5.7 the results are reported, and can help to understand better the process. The calibration points (the red dots) are the probe responses (represented in the complex plane) to the single emitting antenna, that spanned 50 amplitude settings and 50 phases (covering the whole 360° circle). We can already notice that there is a non linearity from there; given a phase, the points are not laying on a line passing from the center of the circle, instead they are deviating from

that while changing the amplitude settings. The blue crosses are the arbitrary targets, whose only requirement is to stay within the calibration points: doing so, each target lays in a triangle whose vertexes are the calibration points closest to the target. The predicted settings to achieve the target is the (rounded) linear combination of the settings of the vertexes of the triangle in which the target is laying in. The linear (affine) model in this case is just a simple line $y = mx + q$ as it is an 1-dimensional problem: y is the target and x is the setting as we are using only one probe and one emitting antenna. m and q are the parameters found via Least Square optimization using the calibration points. The linear model is used for performance comparison between Triangularization and Linear Assumption strategies.

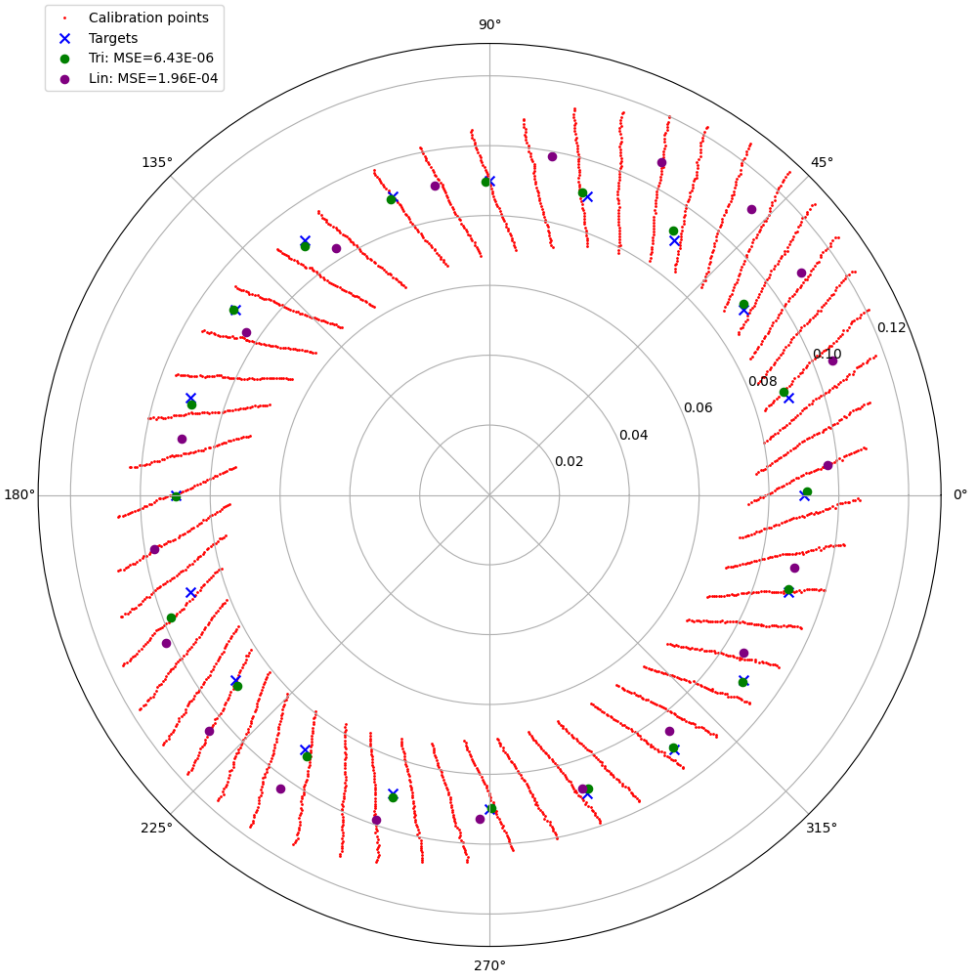

Figure 5.7: Triangularization Results

We can see from Fig. 5.7 that with the triangularization method we are much

more precise in finding the correct setting, but still, even with the linear method, we are not totally far from the targets. This somehow justifies why also with the linear approximation we are obtaining some good results.

5.3 Considerations on the choice of V

As said before, the core requirement of the matrix V to be used is its invertibility. Other practical considerations are:

1. **Amplitude/phase constraints**: each element v_{ij} is a beam former setting, and so can't be arbitrary in terms of both phase and amplitude as it is constrained by the beam former design. In practice, it would be sufficient to predominantly change the phases, and maybe use just a handful of different amplitude settings.

2. **Transmitter dynamic range constraint**: we have limitations in the DUT RX testing, as some required settings of the PAS would be unfeasible due to its dynamic range. This plays an important role especially when using commercial beamformers as a PAS, like the NXP antenna.

3. **Receiver dynamic range constraint**: in the TX case, we need to be sure that each reading $\boldsymbol{r}(\boldsymbol{w})$ to be within the instrumentation limit. Given an instrumentation power constraint P_{const} (at the receiver side), this condition can be translated into

$$|\sum_{k=1}^{N} v_{ik} p_k(\boldsymbol{w})|^2 \leq P_{const} \quad \forall i \in [1, ..., N] \quad \text{and} \quad \forall \boldsymbol{w} \tag{5.12}$$

   A sufficient condition for 5.12 can be:

$$\sum_{k=1}^{N} |v_{ik}|^2 \leq \frac{P_{const}}{N P_{max}} \quad \forall i \in [1, ..., N] \tag{5.13}$$

   where P_{max} is the maximum power that the single element antenna can deliver. A lower bound on the settings can be given by the beamformer noise level, ADC spurious-free dynamic range (SFDR), etc...

4. **Orthogonality**: if we require the rows of V to be orthogonal, then each element of $\boldsymbol{r}(\boldsymbol{w})$ is a projection of $\boldsymbol{p}(\boldsymbol{w})$ on an orthogonal basis (spanned by the rows of $\boldsymbol{V}$). This might help in the M estimation, as the Least Square estimator is optimal if the noise affecting each measurement is independent from the noise of the others (regardless the noise statistic). Given a noisy measurement $\tilde{\boldsymbol{p}}(\boldsymbol{w}) = \boldsymbol{p}(\boldsymbol{w}) + \boldsymbol{e}$, we would like to have its corresponding vector $\tilde{\boldsymbol{r}}(w) = \boldsymbol{V}\tilde{\boldsymbol{p}}(\boldsymbol{w}) = \boldsymbol{r}(\boldsymbol{w}) + \boldsymbol{e'}$ to have each component affected by uncorrelated noise components, i.e. $E(e'_i e'_j) = 0 \quad \forall i, j, i \neq j$.

This can be obtained if $\boldsymbol{V}$ is an orthogonal matrix, in fact:

$$e'_i = \boldsymbol{v}_i^T \boldsymbol{e} \quad e'_j = \boldsymbol{v}_j^T \boldsymbol{e} \quad \Rightarrow E(e'_i e'_j) = 0 \quad \text{since} \quad \boldsymbol{v}_i^T \cdot \boldsymbol{v}_j = 0 \quad \forall i, j, i \neq j \tag{5.14}$$

Note that this doesn't guarantee the measurements to be independent, as being uncorrelated is only a necessary condition for independency.

A kind of matrix that would satisfy all the three conditions is the Hadamard Matrix, which is a square matrix made by 1 and -1 whose rows are orthogonal. It can be adapted to comply with both conditions 1 and 2 just via a simple scale. A complete dissertation on the Hadamard theory, way beyond the scope of this chapter, can be found in [7].

5.4 Further improvements

Polynomial Fit

The first improvement that can be done is a further calibration to find the true non-linear mapping between DUT settings and probes output. Various attempts were carried out, the first one was to use a polynomial model to fit the data instead of a linear one. This lead to overfitting issues with the data and worse performances compared to the linear model. One can then try to perform a Ridge Regression (i.e., regularized polynomial Least Square solution) on the data and see if it is possible to achieve better results. Other ML techniques have been tried out in the past but did not work as expected. This might be due to the fact that the datasets used contained only single element measurements, thus the model was not able to trace back the correct setting as the couplings with the elements were not taken into account. One thing that is worth trying is to increase the dataset with also actual multi-element beams and try with more powerful models.

Repeated measurements technique

Another issue is the dynamic range limitation and the discretization of the possible setting space. For this solution to work it is crucial to have *linearity* of the whole system, both PAS and DUT. The idea is then drive the BF PAS multiple times to achieve the same effect that an infeasible setting would have produced.

We can generalize (5.8) to comply with an infeasible BF setting $\boldsymbol{v}_i$ by writing:

$$\boldsymbol{p} = \boldsymbol{v}_i \cdot a_{in} = \boldsymbol{V}_f \cdot \boldsymbol{q} \cdot a_{in} = (q_1 \boldsymbol{v}_{f,1} + ... + q_N \boldsymbol{v}_{f,N}) \cdot a_{in} \tag{5.15}$$

Each column $\boldsymbol{v}_{f,i}$ of $\boldsymbol{V}_f$ contains a feasible setting, while the vector $\boldsymbol{q}$ contains the weighting of the intermediate results. Thanks to the linearity of the whole system we can in fact record the results produced by each feasible BF setting $\boldsymbol{v}_{f,i}$, and then sum them up using their corresponding weights q_i. In order to find the matrix $\boldsymbol{V}_f$ and weighting vector $\boldsymbol{q}$ we need to solve the constrained convex optimization problem:

$$\begin{cases} \boldsymbol{V}_f, \boldsymbol{q} = argmin_{\boldsymbol{A},\boldsymbol{t}} \|\boldsymbol{p} - \boldsymbol{A} \cdot \boldsymbol{t} \cdot a_{in}\| \\ \boldsymbol{A}_{i,j} \in \boldsymbol{S},\ \boldsymbol{t} \in \mathbb{R}^N \end{cases} \tag{5.16}$$

where $\boldsymbol{S}$ is the set of the feasible settings.

5.5 Conclusions

We can compare Fig.5.5 and the weighting factors obtained in the DUT RX experiment in table 3.1, where only one DUT antenna was active. Even though in the latter case we were observing the NF readings through the eye of the DUT, we see that the error on the isolation among the elements and phase/amplitude discrepancy is comparable with the results of the BF PAS. This might suggest that probably we are already able to obtain similar results of the VSTs even with the linear approximation of the NXP as a BF PAS. The next step would be to replace the VSTs with the NXP and try to reconstruct with that. The only issue is that we cannot perform a calibration as done in 5.8 as we cannot listen to the RX antenna outputs separately to get the NF indication $\boldsymbol{p}$ (and so the matrix $\boldsymbol{P}$ used for calibrating the system). In order to reconstruct then the single DUT antenna outputs (i.e., one column of $\boldsymbol{P}$) we can exploit 5.7 and measure N times (using the *same* BF PAS setting) with different beam-forming settings of the DUT. Doing so we are able to map settings of the BF PAS to realized situations in the NF (seen with the eye of the DUT). Moreover, one could generalized to the multidimensional case (i.e., multiple probes and multiple emitting antennas) the triangularization technique and use that in place of the linear model.

6

Conclusions and Future Works

This chapter briefly outlines the results of the experiments, namely Generalized PAS of Chapter 3, RX Pattern Reconstruction Algorithm of Chapter 4 and Beam Formed PAS of Chapter 5. Moreover some suggestions on the future developments of the technology is given.

6.1 Conclusions of the Generalized PAS Experiment

The objective of this experiment was demonstrating the PAS insensibility to the DUT structure, as from the scalability point of view building a PAS for each DUT's type is not affordable. To do that, the NXP DUT with the Scarif PAS and the Scarif DUT with the NXP PAS were measured and, in the best case scenario, the reconstructions should be the same as if their ad-hoc PASs were used. The main conclusions are:

1. PAS design doesn't have to be very specific to the DUT
2. Using more than the minimum number of probe elements is possible.
3. Moving probes farther away from the active DUT elements seems to make readings less reliable and reduces reconstruction performance.
4. Measurements on DUTs with active immutable elements (e.g., the Scarif) seem to be sensitive to the specific probe selection. It is not yet clear the reason behind this behavior; the most probable explanation is that the Scarif DUT is a not commercial proof of concept antenna while the NXP DUT is a much more reliable and tested device.

The main limitation of this experiment is the little number of tested DUTs, consequently in order to rule out bugs of the system one should increase the DUTs statistic.

6.2 Conclusions of the RX Pattern Reconstruction Algorithm

The reasons behind the development of the new algorithm are essentially two. The first one is that it is faster: in many cases, we have less antennas than the points we want to evaluate the pattern. The second one concerns the feasibility of the two algorithms: it is easier to stimulate one antenna per time than obtaining the effect of multiple plane waves coming from different directions. Still, this is a conjecture as it has not yet proved. A hint in this direction is that it seems that the new algorithm is more accurate in the reconstructions, and in the worst case behaves the same as the Sparse Point RX reconstruction algorithm. Overall the new algorithm seems to work and has good performances. Still, it was not sufficiently tested due to time constraint. For the future development it is important to test the reconstructions with more beams, different frequencies, different power settings and also with different DUTs as only the Scarif was used due to practical/mechanical issues with the fixture with the active PAS.

6.3 Conclusions of the Beam Formed PAS

In DUT RX testing, at the current implementation, we need a number of instrumentation channels at least equal to the number of antennas of the DUT. This is a huge problem, for the cost of the system. The solution to this is having a beamformer at PAS side, and using a single instrumentation line to drive the PAS. In Chapter 5 a mathematical proof on the feasibility of the approach is given for both TX and RX testing scenarios. Moreover, the NXP DUT was used as BF PAS and some experiments were carried out. In the first place, linearity between NXP amplitude/phase settings and realized antenna outputs are assumed. The "BF PAS" (i.e., the NXP DUT) was driven to target each "DUT antenna" (i.e., the VST) in order to stimuli each antenna separately and with the same excitation. In the worst case, isolation of $\sim 17dBV$ between target and other elements was achieved as well as an error of $\sim 3-4dBV$ between targets. A study to characterize the

validity of the linearity assumption was also performed, showing that changing the amplitude has a non linear impact on the realized phase and vice versa. Future work might be to abandon the linearity assumption and find the non linear mapping between DUT settings and realized antenna outputs. In this sense, an experiment was carried out using triangularization techniques aiming to obtain a target situation in the near field. Results were really good and better than the linear mapping approximation. The next steps to take are generalizing the triangularization technique to the multidimensional case, i.e. using multiple emitting antennas and multiple probes. Finally, we can use the NXP DUT to measure another DUT (e.g., the Scarif) and see if we are able to obtain similar results when using multiple VST systems.

7

Appendix A: Measurement Model and Procedure

In this appendix, we will explain the measurement model used in the processing scripts and the steps to be carried out for the TX FF pattern reconstruction.

7.0.1 Phase 1: Calibration

Given a good known device of the same type of the devices to be tested, we perform subsequent measurements in order to obtain:

1. The single element FF pattern $f_n(\theta, \phi)$
2. The calibration matrix $\boldsymbol{G}$ that relates the NF measurements to the weighting factors $\boldsymbol{c}(\boldsymbol{w})$ that are exploited in the FF reconstruction.

7.0.2 Step 1.1: single element FF pattern

In order to estimate $f_n(\theta, \phi)$ for each antenna, we need a probe antenna in the FF that samples the pattern at the points of interest. Furthermore, we need to choose a specific setting $\boldsymbol{w}$ such that only one antenna per time is emitting, while the others are shut down. We can then relate $f_n(\theta, \phi, w_0)$ to the probe antenna reading $b(\theta, \phi, w_0)$ through the equation

$$b(\theta, \phi, w_0) = h_{pr} f_n(\theta, \phi, w_0) \tag{7.1}$$

where:

- h_{pr} is a constant representing all the possible couplings between the electric field in the probe position and the signal at the probe output port itself (impedance and polarization matching, effective length, reflections...)
- w_0 is the setting of such antenna, that we can call *reference setting* respect to which each measurement in the FF will be referred to.

Both h_{pr} and w_0 are independent from the emitting antenna. Said so, we can write the relation between antenna reading and FF patterns as

$$b(\theta, \phi, w_0) \simeq f_n(\theta, \phi, w_0) \tag{7.2}$$

in the sense that we can ignore h_{pr} as it will be then calibrated out when determining the calibration matrix $\boldsymbol{G}$. We need to point out that to perform these measurements the DUT is put into an anechoic chamber, fixed to a moving positioner while the probe orientation and position are fixed. Consequently, h_{pr} can be treated as a complex constant position independent. The dependency of the whole FF pattern of the settings $\boldsymbol{w}$ will be captured by the $\boldsymbol{c_n}$ coefficients, that will be estimated in the next step. Note that it is not possible to rigorously measure the single element pattern, as we would need to decouple completely the effect of the settings from the measurement. Still, the single element measurements are referred to the reference setting so we are actually measuring $f_n(\theta, \phi, w_0)$. We can ignore for the moment w_0, as its impact will be taken into account later on (see (7.1)) . There are two aspects that need to be taken into consideration. The first is that in general the electric field is dual polarized, and this can be treated by performing two measurements, one per electric field component assuming there is not correlation between the two. Given two polarization planes θ and ϕ, we obtain:

$$\begin{aligned} f_{n,\theta}(\theta, \phi) &= b_\theta(\theta, \phi) \\ f_{n,\phi}(\theta, \phi) &= b_\phi(\theta, \phi) \end{aligned} \tag{7.3}$$

The second remark is that for some DUT it is not possible to completely shut down some elements. This issue is solved by performing an interference compensation scheme in which we measure the electric field with two settings: $\boldsymbol{w_n} = [w_{1,off}, ..., w_n, ..., w_{N,off}]$ and $\boldsymbol{w_{off}} = [w_{1,off}, ..., w_{N,off}]$. The setting $w_{i,off}, i = 1, ..., N$ is a special setting in which the i-th element is set at its "minimum possible emission". We can then subtract from the measurement obtained

using $\boldsymbol{w_n}$ the one using $\boldsymbol{w_{off}}$, i.e., an interference compensation. To be more precise, $\boldsymbol{w_{off}}$ not necessarily mean that all the elements are at the minimum emission they can support. It is sufficient that the interfering elements are in a known state (the "off" state) to perform the interference compensation later on.

7.0.3 Step 1.2: weighting factors $\boldsymbol{c(w)}$

The objective of this step is estimating the weighting factors $c_n(w_n)$ for each antenna, and for each set of settings in which one antenna is radiating while the others are turned off (we will relax this condition later). For instance, if we want to estimate the $c_1(\boldsymbol{w})$ coefficients, we will feed the array with all the settings $\boldsymbol{w}$ of the type $\boldsymbol{w} = [w_i, 0, ..., 0]$, where w_i is a general amplitude-phase setting for antenna 1. Note that in principle we have as many coefficients for the target antenna as the number of amplitudes and phases available for that antenna. We can then find the target weighting factor by dividing the measurement in the FF with a certain setting $\boldsymbol{w_i}$ with the FF pattern of the i-th antenna. For the case of antenna 1 this corresponds to:

$$c_1(w_1) = \frac{b(\theta, \phi)|_{\boldsymbol{w=w_1}}}{b(\theta, \phi)|_{\boldsymbol{w=w_0}}} \tag{7.4}$$

where $\boldsymbol{w_0}$ is the same reference setting as before. Since these coefficients are not dependent on the position, we can choose a (θ_0, ϕ_0) to reduce the measurement errors and keep it fixed. We can then associate to a certain $\boldsymbol{w_i}$ a weighting vector $\boldsymbol{c_i(w_i)} = [0, ..., 0, c_i(w_i), 0, ..., 0]$ containing the coefficients to weight the single element patterns in the FF. Since with the setting $\boldsymbol{w_i}$ we are exciting the i-th antenna only, then all the other coefficients are 0.
We can extend this reasoning also in the case in which we can't completely turn off the elements. To do so we can apply the same reasoning of the precedent step, and so estimating the interference and then subtracting it from our measurements, i.e.:

$$c_1(w_1) = \frac{b(\theta, \phi)|_{\boldsymbol{w=w_1}} - b(\theta, \phi)|_{\boldsymbol{w=w_{off}}}}{b(\theta, \phi)|_{\boldsymbol{w=w_0}}} \tag{7.5}$$

Note that in this context $\boldsymbol{w_1} = [w_1, w_{off}, ..., w_{off}]$ (while without interference we had $\boldsymbol{w_1} = [w_1, 0, ..., 0]$). Consequently, we can associate to the setting $\boldsymbol{w_i}$ the realized weighting vector $\boldsymbol{c_i(w_i)} = [c_{1,off}, ..., c_i(w_i), c_{i+1,off}, ..., c_{N,off}]$.

In (7.8) we have the demonstration that, with this single element pattern and weighting factors pseudo-estimation, we are actually reconstructing the target pattern of (2.4).

7.0.4 Step 1.3: NF PAS measurements $\boldsymbol{p(w)}$

The purpose of this step is obtaining the NF PAS indications. The PAS has the same number of probes as the DUT array (N), and for each setting $\boldsymbol{w}_k$ it returns N coefficients at its output ports forming the vector $\boldsymbol{p}_k = [p_{1,k}, ..., p_{N,k}]$. As explained before, the objective is estimating the linear relation between these PAS indications $\boldsymbol{p}$ and weighting factors $\boldsymbol{c}$, i.e. the NxN matrix $\boldsymbol{G}$. To do so it would be sufficient to perform N measurements, each one with different $\boldsymbol{w}_k$ to obtain the corresponding $\boldsymbol{c}_k$ and $\boldsymbol{p}_k$ vectors. For the linearity assumption $\boldsymbol{c}_k = \boldsymbol{G}\boldsymbol{p}_k$, consequently we can write as done in 2.5:

$$\boldsymbol{C} = \boldsymbol{G}\boldsymbol{P} \tag{7.6}$$

where the k-th column of $\boldsymbol{C}$ and $\boldsymbol{P}$ are the vectors $\boldsymbol{c}_k$ and $\boldsymbol{p}_k$ respectively. We can obtain $\boldsymbol{G}$ by simply invert $\boldsymbol{P}$, i.e. $\boldsymbol{G} = \boldsymbol{P}^{-1}\boldsymbol{C}$. The existence of $\boldsymbol{P}^{-1}$ is guaranteed by a (wise) choice of the settings $\boldsymbol{w}_k$. This method has two problems:

1. We are not taking into account the noise.
2. A wise choice of $\boldsymbol{w}_k$ is not easy to obtain since different $\boldsymbol{w}_k$ might result into the same $\boldsymbol{p}_k$ and $\boldsymbol{c}_k$.

What can we do, and what is done in practice, is solving a least square minimization problem with an overestimated system of equations spanning a sufficiently large set of possible settings as explained in the next step.

7.0.5 Step 1.4: Calibration Matrix G

Given the weighting factor $\boldsymbol{C}$ and the NF measurements $\boldsymbol{P}$ matrices, that have dimensions NxK where N is the number of DUT/PAS antennas and K is the total number of settings we calibrate with, we can find the Calibration matrix $\boldsymbol{G}$ via Least Square minimization as described in 2.2.1. In particular we want to minimize the regression residue $\epsilon(\boldsymbol{A}) = ||\boldsymbol{C} - \boldsymbol{AP}||$. We need to solve then:

$$\begin{aligned} \tilde{\boldsymbol{G}} &= argmin_{\boldsymbol{A}}\epsilon(\boldsymbol{A}) = argmin_{\boldsymbol{A}}||\boldsymbol{C} - \boldsymbol{AP}|| \\ &= argmin_{\boldsymbol{A}}\sqrt{\sum_{i=1}^{N}\sum_{j=1}^{K}|(\boldsymbol{C} - \boldsymbol{AP})_{ij}|^2} \end{aligned} \tag{7.7}$$

very much similar to (2.2.1).

7.0.6 Phase 2: DUT measurement

We can then exploit the results of Phase 1 to reconstruct the far field of a given DUT of the same type of one used for calibration. The steps are:

1. Measure with the PAS the NF coefficients $\boldsymbol{p}(\boldsymbol{w})$

2. Use the matrix $\boldsymbol{G}$ in Step 1.4 to estimate the weighting factors $\boldsymbol{c}(\boldsymbol{w})$ with $\boldsymbol{c}(\boldsymbol{w}) = \boldsymbol{G}\boldsymbol{p}(\boldsymbol{w})$

3. Exploit the $\boldsymbol{c}(\boldsymbol{w})$ coefficients and the single element FF pattern of Step 1.1 of the calibration to reconstruct the DUT FF pattern using (2.4):

$$E(\theta, \phi, \boldsymbol{w}) = \sum_{n=1}^{N} c_n(w_n) f_n(\theta, \phi)$$

In the figure below an high level scheme of the measurement procedure is reported.

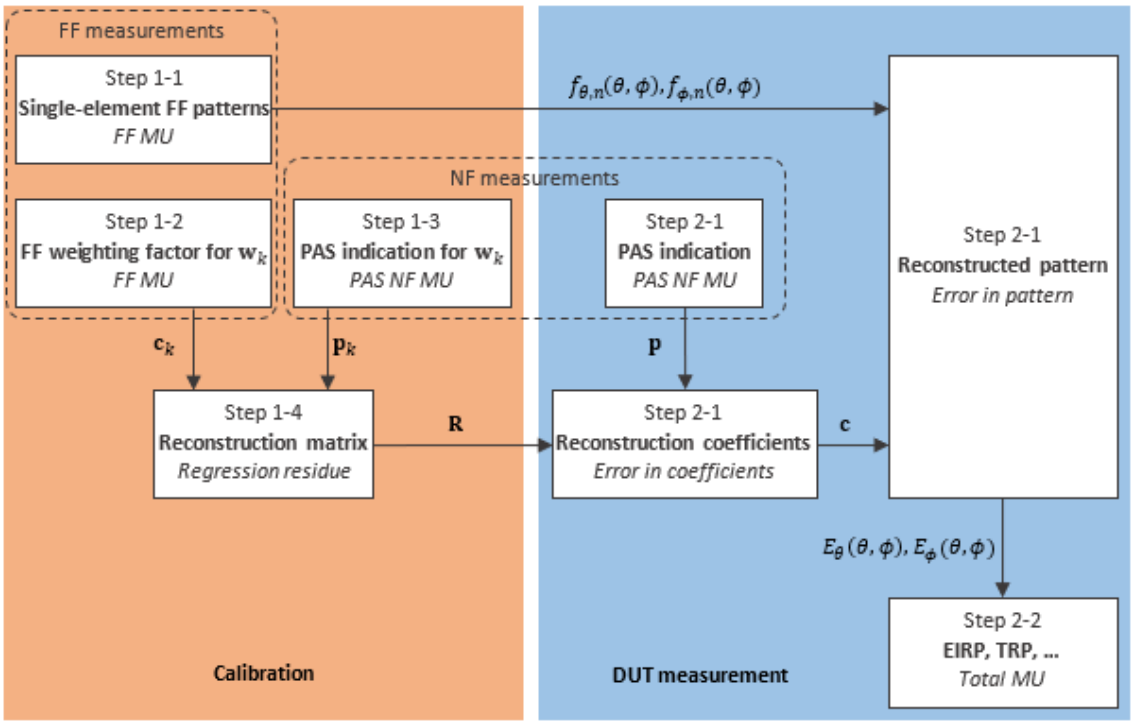

Figure 7.1: Procedure Schema

7.1 Impact of the reference setting w_0

As mentioned before, it is not possible to completely separate the impact of the settings from the single element FF pattern. Here we demonstrate that with this "pseudo estimation" of the single-element patterns and weighting factors we obtain our goal. If we rewrite equation (2.4) with the single element patterns and weighting factors estimated in steps 1.1 and 1.2 respectively, we obtain:

$$\begin{aligned}\sum_{n=1}^{N} c_n(w_n) f_n(\theta,\phi,w_0) &= \sum_{n=1}^{N} \frac{b(\theta_0,\phi_0)|_{w=w_n}}{b(\theta_0,\phi_0)|_{w=w_0}} f_n(\theta,\phi,w_0) \\ &= \sum_{n=1}^{N} \frac{f_n(\theta_0,\phi_0,w_n)}{f_n(\theta_0,\phi_0,w_0)} f_n(\theta,\phi,w_0)\end{aligned} \tag{7.8}$$

If we now expand the terms using the definition of $f_n(\theta,\phi,w_n)$ in (2.4) and simplify the common terms we will end up with

$$\sum_{n=1}^{N} c_n(w_n)\sqrt{D_n(\theta,\phi)}e^{-jk\Delta d_n(\theta,\phi)} = E(\theta,\phi,w_n) \tag{7.9}$$

which is exactly what we want to measure. Thus, the choice of the reference setting with which we choose to measure does not have an impact on the estimation, which is independent on that. Still, the choice of a good reference setting does have an impact on the SNR mainly through the radiated power that is configured.

8

Appendix B: Simple Calibration

As an alternative to the procedure presented in the DUT TX case testing, there exist an equivalent method to achieve the same results called "Simple Calibration". The word simple refers to the mathematical structure needed, which in this procedure is simpler with respect to the previous case. In the Simple Calibration we impose linearity between the Near Field readings $\boldsymbol{p}(\boldsymbol{w})$ and the Far Field readings without the need of the weighting factors $\boldsymbol{c}(\boldsymbol{w})$. We can now proceed to derive the model and procedure of this method.

8.1 Model Derivation

Here we derive two models, one for the Far Field measurements and one for the Near Field. These models will be then linked together in the calibration section.

8.1.1 Far Field measurements model

We can recall 2.4 and write the normalized electric field in the Far Field as

$$E(\theta, \phi, \boldsymbol{w}) = \sum_{n=1}^{N} c_n(\boldsymbol{w}) f_n(\theta, \phi)$$

The electric field can be *directly* related to the probe reading $b(\theta, \phi, \boldsymbol{w})$ through the coupling factor h_{pr} as described in the previous chapter obtaining:

$$\begin{aligned} b(\theta, \phi, \boldsymbol{w}) &= h_{pr} \cdot E(\theta, \phi, \boldsymbol{w}) \\ &\simeq E(\theta, \phi, \boldsymbol{w}) = \sum_{n=1}^{N} c_n(\boldsymbol{w}) f_n(\theta, \phi) \end{aligned} \tag{8.1}$$

where the $\simeq$ is valid assuming will be able to calibrate out the probe effect in the calibration procedure, as discussed in Appendix A. It's important to notice that the $b(\theta, \phi, \boldsymbol{w})$ coefficients depend now on $\boldsymbol{w}$, while in the previous chapter they were independent of the settings: we are capturing the $c_n(\boldsymbol{w})$ coefficients effect directly into the probe reading. If we now sample the FF readings in L points, we can rewrite the function $b(\theta, \phi, \boldsymbol{w})$ in vectorial form obtaining the vector:

$$\boldsymbol{b}(\boldsymbol{w}) = [b(\theta_1, \phi_1, \boldsymbol{w}), ..., b(\theta_L, \phi_L, \boldsymbol{w})]^T$$

We can further decouple the effect of the input signal at each DUT antenna from its resulting FF pattern, and so rewriting $f_n(\theta, \phi)$ as:

$$f_n(\theta, \phi) = f_{FF,n}(\theta, \phi) \cdot a_{in} \tag{8.2}$$

Doing so we can interpret $f_{FF,n}$ as the transfer function between the DUT input signal a_{in} (that is the same for each DUT antenna) and the FF pattern of each antenna. We can now rewrite 8.1 in matrix form

$$\boldsymbol{b}(\boldsymbol{w}) = \boldsymbol{F}_{FF} \cdot \boldsymbol{c}(\boldsymbol{w}) \cdot a_{in} \tag{8.3}$$

where

- $\boldsymbol{F}_{FF} = \begin{bmatrix} f_{FF,1}(\theta_1, \phi_1) & \cdots & f_{FF,N}(\theta_1, \phi_1) \\ \vdots & \ddots & \vdots \\ f_{FF,1}(\theta_L, \phi_L) & \cdots & f_{FF,N}(\theta_L, \phi_L) \end{bmatrix}$ is an LxN matrix and contains the single element Far Field transfer functions sampled in L points
- $\boldsymbol{c}(\boldsymbol{w}) = [c_1(\boldsymbol{w}), ..., c_N(\boldsymbol{w})]^T$ contains the FF weighting factors of each antenna $1, ..., N$

8.1.2 Near Field measurements model

The idea is to model the NF readings in a similar way as done in the FF. In particular if we have M probes, we can model each probe reading $p_m(\boldsymbol{w})$ as:

$$p_m(\boldsymbol{w}) = \sum_{n=1}^{N} c_n(\boldsymbol{w}) f_{NF,m,n} a_{in} \tag{8.4}$$

The $f_{NF,m,n}$ is the transfer function between the DUT element n and the PAS probe m. Note that both the $c_n(\boldsymbol{w})$ and a_{in} coefficients are the same as the FF case as we are keeping the same input and settings for both NF and FF measurements. Note that "same settings" doesn't mean that we are keeping the settings fixed to a constant, but that the couple $\boldsymbol{b}(\boldsymbol{w})$ and $\boldsymbol{p}(\boldsymbol{w})$ is found using the same $\boldsymbol{w}$ and changing it would lead to different pairs of $\boldsymbol{b}(\boldsymbol{w})$ and $\boldsymbol{p}(\boldsymbol{w})$. We can now rewrite 8.4 in matrix form:

$$\boldsymbol{p}(\boldsymbol{w}) = \boldsymbol{F}_{NF} \cdot \boldsymbol{c}(\boldsymbol{w}) \cdot a_{in} \tag{8.5}$$

where:

$$\boldsymbol{F}_{NF} = \begin{bmatrix} f_{NF,1,1} & \cdots & f_{NF,1,N} \\ \vdots & \ddots & \vdots \\ f_{NF,M,1} & \cdots & f_{NF,M,N} \end{bmatrix}$$

is an MxN matrix and contains the single element NF transfer functions.

8.1.3 Near Field to Far Field calibration matrix

Starting from equation 8.5 we can find the weighting factors $\boldsymbol{c}(\boldsymbol{w})$ as:

$$\boldsymbol{c}(\boldsymbol{w}) = (\boldsymbol{F}_{NF}^T \boldsymbol{F}_{NF})^{-1} \boldsymbol{F}_{NF}^T a_{in}^{-1} \boldsymbol{p}(\boldsymbol{w}) \tag{8.6}$$

and substitute it into 8.3 obtaining:

$$\begin{aligned} \boldsymbol{b}(\boldsymbol{w}) &= \boldsymbol{F}_{FF} (\boldsymbol{F}_{NF}^T \boldsymbol{F}_{NF})^{-1} \boldsymbol{F}_{NF}^T \boldsymbol{p}(\boldsymbol{w}) \\ &= \boldsymbol{G} \boldsymbol{p}(\boldsymbol{w}) \end{aligned} \tag{8.7}$$

with $\boldsymbol{G} = \boldsymbol{F}_{FF} (\boldsymbol{F}_{NF}^T \boldsymbol{F}_{NF})^{-1} \boldsymbol{F}_{NF}^T$ as the NF to FF calibration matrix. There are some properties of G that are worth pointing out:

- Its dimensions are LxM, where L is the number of points in the FF we are interested in and M is the number of PAS antennas.
- Since we have N emitting antennas, we potentially have N degrees of freedom in input, and this implies that the image space of G has at most dimension N. It is exactly equal to N only if $L \geqslant N$ and $M \geqslant N$, and if this is the case we could in principle reconstruct any FF pattern, that has dimension N.
- $L \geqslant N$ and $M \geqslant N$ are only necessary conditions for $\boldsymbol{G}$ to be full rank. We need rank($\boldsymbol{F}_{NF}$) $\geq N$ to reconstruct any FF patterns, and this translates into requiring each PAS-to-DUT antennas' transfer function to be sufficiently independent one another. One could apply the same reasoning for the FF matrix for the $L \geqslant N$ condition , and so requiring that rank($\boldsymbol{F}_{FF}$) $\geqslant N$, but the column of $\boldsymbol{F}_{FF}$ are linearly independent by construction (by choosing different observation points in each column). If one is interested in having less FF points than N, then $\boldsymbol{G}$ wouldn't be full rank but would predict correctly each pattern in the required lower dimensional FF space.

In order to estimate $\boldsymbol{G}$ a Least Square Approach is performed, very much similar as done in the TUD calibration procedure. The key difference is that now there's a different target, as we are no longer mapping NF indications $\boldsymbol{p}(\boldsymbol{w})$ to weighting factors $\boldsymbol{c}(\boldsymbol{w})$ but we map them directly to FF indications $\boldsymbol{b}(\boldsymbol{w})$. We can then define the FF indications matrix:

$$\boldsymbol{B} = [\boldsymbol{b}(\boldsymbol{w_1}), ..., \boldsymbol{b}(\boldsymbol{w_p})] \tag{8.8}$$

containing p FF measured patterns each of them with different configuration settings. Similarly we can define the NF measurement matrix:

$$\boldsymbol{P} = [\boldsymbol{p}(\boldsymbol{w_1}), ..., \boldsymbol{p}(\boldsymbol{w_p})] \tag{8.9}$$

and rewrite 8.7 as:

$$\boldsymbol{B} = \boldsymbol{GP} \tag{8.10}$$

To find $\boldsymbol{G}$ we can solve:

$$\boldsymbol{G} = argmin_{\boldsymbol{A}} ||\boldsymbol{B} - \boldsymbol{AP}||^2 \tag{8.11}$$

whose solution is

$$\boldsymbol{G} = \boldsymbol{BP}^{\dagger} \tag{8.12}$$

with $\boldsymbol{P}^{\dagger}$ the pseudo-inverse of $\boldsymbol{P}$.

References

[1] Jeffrey G. Andrews et al. "What Will 5G Be?" In: *IEEE Journal on Selected Areas in Communications* 32.6 (2014), pp. 1065–1082. DOI: 10.1109/JSAC.2014.2328098.

[2] Constantine A Balanis. *Antenna theory: analysis and design*. John wiley & sons, 2016.

[3] Adrian Constantin and R. Johnson. "Large gyres as a shallow-water asymptotic solution of Euler's equation in spherical coordinates". In: *Proceedings of the Royal Society A: Mathematical, Physical and Engineering Science* 473 (Apr. 2017), p. 20170063. DOI: 10.1098/rspa.2017.0063.

[4] Lei Dong et al. "Introduction on IMT-2020 5G trials in China". In: *IEEE Journal on Selected Areas in Communications* 35.8 (2017), pp. 1849–1866.

[5] Mattias Gustafsson, Tommi Jämsä, and Mats Högberg. "OTA methods for 5G BTS testing — Survey of potential approaches". In: *2017 XXXIInd General Assembly and Scientific Symposium of the International Union of Radio Science (URSI GASS)*. 2017, pp. 1–4. DOI: 10.23919/URSIGASS.2017.8105369.

[6] T. Hirvonen, J. Tuovinen, and A. Raisanen. "Lens-Type Compact Antenna Test Range at MM-Waves". In: *1991 21st European Microwave Conference*. Vol. 2. 1991, pp. 1079–1083. DOI: 10.1109/EUMA.1991.336489.

[7] Kathy J Horadam. *Hadamard matrices and their applications*. Princeton university press, 2012.

[8] Per-Simon Kildal. "OTA measurements of wireless stations in reverberation chamber versus anechoic chamber: from accuracy models to testing of MIMO systems". In: *2010 International Workshop on Antenna Technology (iWAT)*. 2010, pp. 1–4. DOI: 10.1109/IWAT.2010.5464859.

[9] Per-Simon Kildal and Andrés Alayón Glazunov. "OTA testing of 3G-5G devices with MIMO: From anechoic chambers to reverberation chambers and . . . back again?" In: *2017 IEEE International Symposium on Antennas and Propagation & USNC/URSI National Radio Science Meeting*. 2017, pp. 1697–1698. DOI: 10.1109/APUSNCURSINRSM.2017.8072891.

[10] Pekka Kyösti et al. "On Dimensions of OTA Setups for Massive MIMO Base Stations Radiated Testing". In: *IEEE Access* 4 (2016), pp. 5971–5981. DOI: 10.1109/ACCESS.2016.2610721.

[11] Martin Laabs et al. "A Novel OTA Near-Field Measurement Approach Suitable for 5G mmWave Validation and Test". In: *2021 51st European Microwave Conference (EuMC)*. 2022, pp. 564–567. DOI: 10.23919/EuMC50147.2022.9784294.

[12] Der-Tsai Lee and Bruce J Schachter. "Two algorithms for constructing a Delaunay triangulation". In: *International Journal of Computer & Information Sciences* 9.3 (1980), pp. 219–242.

[13] Shao-Yu Lien et al. "5G new radio: Waveform, frame structure, multiple access, and initial access". In: *IEEE communications magazine* 55.6 (2017), pp. 64–71.

[14] Michael Löhning et al. "A Novel OTA Near-Field Measurement Approach Suitable for 5G mmWave Wideband Modulated Tests". In: *2022 IEEE/MTT-S International Microwave Symposium - IMS 2022*. 2022, pp. 856–858. DOI: 10.1109/IMS37962.2022.9865448.

[15] Carlos F. López and Cheng-Xiang Wang. "Novel 3-D Non-Stationary Wideband Models for Massive MIMO Channels". In: *IEEE Transactions on Wireless Communications* 17.5 (2018), pp. 2893–2905. DOI: 10.1109/TWC.2018.2804385.

[16] George R. MacCartney et al. "Path loss models for 5G millimeter wave propagation channels in urban microcells". In: *2013 IEEE Global Communications Conference (GLOBECOM)*. 2013, pp. 3948–3953. DOI: 10.1109/GLOCOM.2013.6831690.

[17] Mattia Maggi et al. "Millimeter-Wave Phased Arrays and Over-the-Air Characterization for 5G and Beyond". In: ().

[18] Gregory F Masters. "Probe-correction coefficients derived from near-field measurements". In: *AMTA Conference, October*. 1991, pp. 7–11.

[19] Philip M Morse. "Feshbach, Methods of theoretical physics". In: *Vol. I, McGraw-Hill, New York. EFFECTIVE MASS APPROXIMATION* 461.7 (1953), p. 437.

[20] Yihong Qi et al. "5G Over-the-Air Measurement Challenges: Overview". In: *IEEE Transactions on Electromagnetic Compatibility* 59.6 (2017), pp. 1661–1670. DOI: 10.1109/TEMC.2017.2707471.

[21] Theodore S. Rappaport et al. "Overview of Millimeter Wave Communications for Fifth-Generation (5G) Wireless Networks—With a Focus on Propagation Models". In: *IEEE Transactions on Antennas and Propagation* 65.12 (2017), pp. 6213–6230. DOI: 10.1109/TAP.2017.2734243.

[22] Kent Rosengren and Per-Simon Kildal. "Study of distributions of modes and plane waves in reverberation chambers for the characterization of antennas in a multipath environment". In: *Microwave and Optical Technology Letters* 30.6 (), pp. 386–391. DOI: https://doi.org/10.1002/mop.1323.

[23] Shintaro Shinjo et al. "Integrating the Front End: A Highly Integrated RF Front End for High-SHF Wide-Band Massive MIMO in 5G". In: *IEEE Microwave Magazine* 18.5 (2017), pp. 31–40. DOI: 10.1109/MMM.2017.2690883.

[24] Mohammad Mehdi Tamaddondar and Narges Noori. "Plane wave against spherical wave assumption for non-uniform linear massive MIMO array structures in LOS condition". In: *2017 Iranian Conference on Electrical Engineering (ICEE)*. 2017, pp. 1802–1805. DOI: 10.1109/IranianCEE.2017.7985344.

[25] L. M. Tancioni et al. "Over-the-Air testing of Active Antenna System Base Stations in Compact Antenna Test Range". In: *2019 13th European Conference on Antennas and Propagation (EuCAP)*. 2019, pp. 1–5.

[26] A. Yaghjian. "An overview of near-field antenna measurements". In: *IEEE Transactions on Antennas and Propagation* 34.1 (1986), pp. 30–45. DOI: 10.1109/TAP.1986.1143727.

[27] Xiaohang Yang et al. "Standardization Progress and Challenges for 5G MIMO OTA Performance Testing". In: *2022 IEEE 5th International Conference on Electronic Information and Communication Technology (ICEICT)*. 2022, pp. 505–507. DOI: 10.1109/ICEICT55736.2022.9908833.

[28] Ping Zhang et al. "A survey of testing for 5G: Solutions, opportunities, and challenges". In: *China Communications* 16.1 (2019), pp. 69–85. DOI: 10.12676/j.cc.2019.01.007.

Acknowledgments

I want to thank my family and friends for bearing me throughout all these years of studying, NI people for welcoming and supporting me during my internship and my professors for preparing me for my professional life. Special thanks go to the Fritz and Buda people for making my Erasmus one of the best experiences of my life, and Höelün for helping me write these Ackowledgments.

References

[1] Jeffrey G. Andrews et al. "What Will 5G Be?" In: *IEEE Journal on Selected Areas in Communications* 32.6 (2014), pp. 1065–1082. DOI: 10.1109/JSAC.2014.2328098.

[2] Constantine A Balanis. *Antenna theory: analysis and design*. John wiley & sons, 2016.

[3] Adrian Constantin and R. Johnson. "Large gyres as a shallow-water asymptotic solution of Euler's equation in spherical coordinates". In: *Proceedings of the Royal Society A: Mathematical, Physical and Engineering Science* 473 (Apr. 2017), p. 20170063. DOI: 10.1098/rspa.2017.0063.

[4] Lei Dong et al. "Introduction on IMT-2020 5G trials in China". In: *IEEE Journal on Selected Areas in Communications* 35.8 (2017), pp. 1849–1866.

[5] Mattias Gustafsson, Tommi Jämsä, and Mats Högberg. "OTA methods for 5G BTS testing — Survey of potential approaches". In: *2017 XXXIInd General Assembly and Scientific Symposium of the International Union of Radio Science (URSI GASS)*. 2017, pp. 1–4. DOI: 10.23919/URSIGASS.2017.8105369.

[6] T. Hirvonen, J. Tuovinen, and A. Raisanen. "Lens-Type Compact Antenna Test Range at MM-Waves". In: *1991 21st European Microwave Conference*. Vol. 2. 1991, pp. 1079–1083. DOI: 10.1109/EUMA.1991.336489.

[7] Kathy J Horadam. *Hadamard matrices and their applications*. Princeton university press, 2012.

[8] Per-Simon Kildal. "OTA measurements of wireless stations in reverberation chamber versus anechoic chamber: from accuracy models to testing of MIMO systems". In: *2010 International Workshop on Antenna Technology (iWAT)*. 2010, pp. 1–4. DOI: 10.1109/IWAT.2010.5464859.

[9] Per-Simon Kildal and Andrés Alayón Glazunov. "OTA testing of 3G-5G devices with MIMO: From anechoic chambers to reverberation chambers and . . . back again?" In: *2017 IEEE International Symposium on Antennas and Propagation & USNC/URSI National Radio Science Meeting*. 2017, pp. 1697–1698. DOI: 10.1109/APUSNCURSINRSM.2017.8072891.

[10] Pekka Kyösti et al. "On Dimensions of OTA Setups for Massive MIMO Base Stations Radiated Testing". In: *IEEE Access* 4 (2016), pp. 5971–5981. DOI: 10.1109/ACCESS.2016.2610721.

[11] Martin Laabs et al. "A Novel OTA Near-Field Measurement Approach Suitable for 5G mmWave Validation and Test". In: *2021 51st European Microwave Conference (EuMC)*. 2022, pp. 564–567. DOI: 10.23919/EuMC50147.2022.9784294.

[12] Der-Tsai Lee and Bruce J Schachter. "Two algorithms for constructing a Delaunay triangulation". In: *International Journal of Computer & Information Sciences* 9.3 (1980), pp. 219–242.

[13] Shao-Yu Lien et al. "5G new radio: Waveform, frame structure, multiple access, and initial access". In: *IEEE communications magazine* 55.6 (2017), pp. 64–71.

[14] Michael Löhning et al. "A Novel OTA Near-Field Measurement Approach Suitable for 5G mmWave Wideband Modulated Tests". In: *2022 IEEE/MTT-S International Microwave Symposium - IMS 2022*. 2022, pp. 856–858. DOI: 10.1109/IMS37962.2022.9865448.

[15] Carlos F. López and Cheng-Xiang Wang. "Novel 3-D Non-Stationary Wideband Models for Massive MIMO Channels". In: *IEEE Transactions on Wireless Communications* 17.5 (2018), pp. 2893–2905. DOI: 10.1109/TWC.2018.2804385.

[16] George R. MacCartney et al. "Path loss models for 5G millimeter wave propagation channels in urban microcells". In: *2013 IEEE Global Communications Conference (GLOBECOM)*. 2013, pp. 3948–3953. DOI: 10.1109/GLOCOM.2013.6831690.

[17] Mattia Maggi et al. "Millimeter-Wave Phased Arrays and Over-the-Air Characterization for 5G and Beyond". In: ().

[18] Gregory F Masters. "Probe-correction coefficients derived from near-field measurements". In: *AMTA Conference, October*. 1991, pp. 7–11.

[19] Philip M Morse. "Feshbach, Methods of theoretical physics". In: *Vol. I, McGraw-Hill, New York. EFFECTIVE MASS APPROXIMATION* 461.7 (1953), p. 437.

[20] Yihong Qi et al. "5G Over-the-Air Measurement Challenges: Overview". In: *IEEE Transactions on Electromagnetic Compatibility* 59.6 (2017), pp. 1661–1670. DOI: 10.1109/TEMC.2017.2707471.

[21] Theodore S. Rappaport et al. "Overview of Millimeter Wave Communications for Fifth-Generation (5G) Wireless Networks—With a Focus on Propagation Models". In: *IEEE Transactions on Antennas and Propagation* 65.12 (2017), pp. 6213–6230. DOI: 10.1109/TAP.2017.2734243.

[22] Kent Rosengren and Per-Simon Kildal. "Study of distributions of modes and plane waves in reverberation chambers for the characterization of antennas in a multipath environment". In: *Microwave and Optical Technology Letters* 30.6 (), pp. 386–391. DOI: https://doi.org/10.1002/mop.1323.

[23] Shintaro Shinjo et al. "Integrating the Front End: A Highly Integrated RF Front End for High-SHF Wide-Band Massive MIMO in 5G". In: *IEEE Microwave Magazine* 18.5 (2017), pp. 31–40. DOI: 10.1109/MMM.2017.2690883.

[24] Mohammad Mehdi Tamaddondar and Narges Noori. "Plane wave against spherical wave assumption for non-uniform linear massive MIMO array structures in LOS condition". In: *2017 Iranian Conference on Electrical Engineering (ICEE)*. 2017, pp. 1802–1805. DOI: 10.1109/IranianCEE.2017.7985344.

[25] L. M. Tancioni et al. "Over-the-Air testing of Active Antenna System Base Stations in Compact Antenna Test Range". In: *2019 13th European Conference on Antennas and Propagation (EuCAP)*. 2019, pp. 1–5.

[26] A. Yaghjian. "An overview of near-field antenna measurements". In: *IEEE Transactions on Antennas and Propagation* 34.1 (1986), pp. 30–45. DOI: 10.1109/TAP.1986.1143727.

[27] Xiaohang Yang et al. "Standardization Progress and Challenges for 5G MIMO OTA Performance Testing". In: *2022 IEEE 5th International Conference on Electronic Information and Communication Technology (ICEICT)*. 2022, pp. 505–507. DOI: 10.1109/ICEICT55736.2022.9908833.

[28] Ping Zhang et al. "A survey of testing for 5G: Solutions, opportunities, and challenges". In: *China Communications* 16.1 (2019), pp. 69–85. DOI: 10.12676/j.cc.2019.01.007.